PDMS-based platforms for in vitro neural cultures and axon guidance

Yanshan Peng

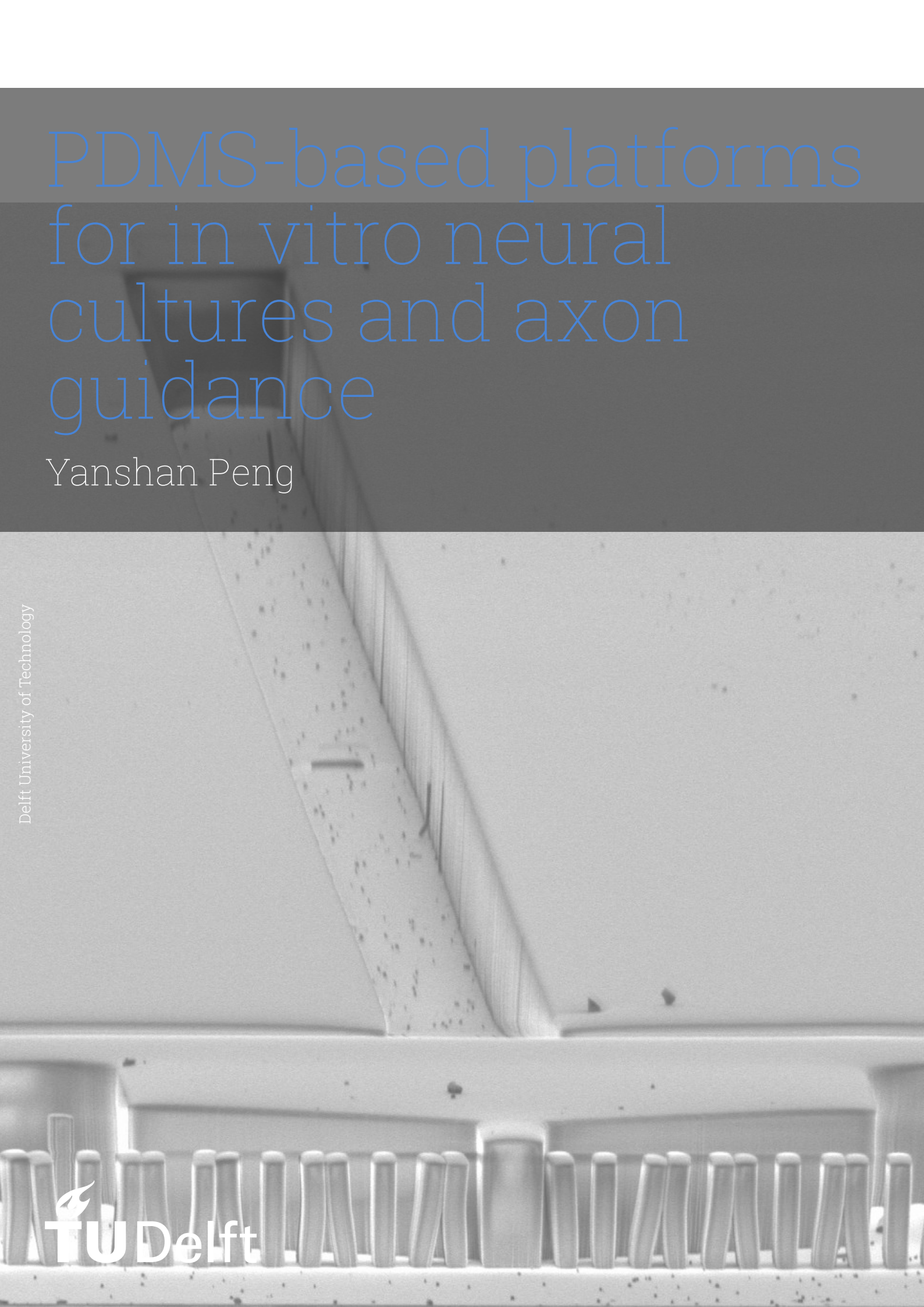

Delft University of Technology

TU Delft

PDMS-based platforms for in vitro neural cultures and axon guidance

by

Yanshan Peng

to obtain the degree of Master of Science
at the Delft University of Technology
to be defended publicly on August 28, 2025, at 10:00

Supervisor :	Dr. Achilleas Savva
Thesis committee:	Dr. Achilleas Savva
	Dr. Paola Fanzio
	Dr. Clementine Boutry
Project Duration:	February, 2025 - August, 2025
Faculty:	Faculty of Mechanical Engineering, Delft

TU Delft

Preface

The writing journey of this thesis has been full of ups and downs and challenges.

I would like to thank everyone for their support. However, I wish to express my special gratitude to several people.

First, I would like to thank my supervisor, Achilleas Savva, for his guidance throughout my project. He was always willing to discuss the topic with me, coordinate with relevant people, and constantly encouraged me to keep moving forward.

I would also like to thank Paola Fanzio and Clementine Boutry for joining my defense committee. My sincere thanks go to Tawab Karim for his support in the cleanroom — his professionalism and helpfulness left a deep impression on me. I am grateful to Yaren Bathaei for her guidance on 3D printing and material preparation, and to Liwen Wang for her advice on scientific illustration and experimental work.

I also thank all the members of the research group for their valuable feedback during the progress of my project, as well as the staff at EKL for the training that enabled me to successfully conduct various experiments.

Finally, I am deeply grateful to my parents and my friends — their companionship and encouragement have always been a driving force that kept me moving forward.

Yanshan Peng
Delft, August 2025

Abstract

Microfluidic platforms that physically guide axons enable controlled studies of neuronal connectivity, injury, and regeneration *in vitro*. This thesis investigates two fabrication routes for Polydimethylsiloxane (PDMS)-based axon-guidance structures: direct ink writing of printable PDMS inks and cleanroom microfabrication using photolithography and DRIE, with the goal of achieving high-aspect-ratio and high-density features suitable for neuronal applications.

Printable PDMS inks were formulated by blending shear-thinning SE1700 with Sylgard 184 at varying ratios and characterized by shear viscosity and oscillatory rheology at 25 °C. SE1700-containing blends exhibited pronounced shear thinning and gel-like behavior ($G' > G''$) in the linear viscoelastic regime. DIW printability was assessed via dual-layer tests and filament-width analysis under different nozzle sizes, speeds, and displacements. The 8:2 ink provided the best balance between extrusion and shape retention; however, multilayer pores still showed sagging or merging depending on overhang span and dose, and dimensional errors on printed microchannels ranged from 32 to 157 µm depending on geometry.

Additionally, microfabrication produced high-aspect-ratio features on silicon using positive and negative routes. PDMS–PDMS double casting from positive molds revealed failure modes—lateral collapse and longitudinal tearing, in dense, narrow structures during demolding. Direct PDMS casting from negative silicon molds improved geometric fidelity and avoided tearing; measured aspect ratio is close to the wafer values and spontaneous collapse was not observed after demolding.

Overall, DIW enables fast, mold-free prototyping but is limited in resolution and multilayer fidelity; microfabrication delivers micron-precision HAR arrays but entails higher process complexity and demolding risks for dense features. The results outline practical design and process for building PDMS platforms that can be further integrated with MEAs for functional neural studies.

Contents

Preface i

Abstract ii

List of Figures v

List of Tables vi

1 Introduction 1
- 1.1 Background and Significance of Neurological Disorders . . . 1
- 1.2 Challenges in Modeling and Treating Neurological Disorders . . . 2
- 1.3 *In Vitro* Platforms in Neuroscience . . . 2
  - 1.3.1 Neuron Sources for *In Vitro* Studies . . . 3
  - 1.3.2 Advantages of *In Vitro* Platforms . . . 3
- 1.4 Microfluidic Platforms for Neuronal Research . . . 3
- 1.5 PDMS as an Ideal Material for Microfluidics and Axon Guidance Structures . . . 4
- 1.6 Fabrication Methods and Their Challenges for PDMS-based Microfluidics . . . 5
  - 1.6.1 Additive Manufacturing . . . 5
  - 1.6.2 Microfabrication . . . 6
- 1.7 Integration of PDMS Axon-Guidance Structures with Microelectrode Arrays (MEAs) . . . 8
- 1.8 Research Question . . . 9

2 Direct Ink Writing of PDMS Structures 11
- 2.1 Materials and Methods . . . 11
  - 2.1.1 Ink Preparation . . . 11
  - 2.1.2 Rheological Characterization . . . 11
  - 2.1.3 Printability Analysis . . . 11
  - 2.1.4 3D Printing of Microfluidics . . . 12
- 2.2 Results . . . 14
  - 2.2.1 Rheological Properties . . . 14
  - 2.2.2 PDMS Printability . . . 18
- 2.3 Discussion . . . 22
  - 2.3.1 Rheological Properties and Their Implications for Printing . . . 22
  - 2.3.2 Factors Affecting PDMS Printability . . . 22
  - 2.3.3 Advantages and Limitations of DIW . . . 23

3 Microfabrication of PDMS Microfluidics 25
- 3.1 Materials and Methods . . . 25
  - 3.1.1 Mask Design . . . 25
  - 3.1.2 Fabrication of the Microfluidic Structures . . . 27
  - 3.1.3 Characterization . . . 28
- 3.2 Results . . . 29
  - 3.2.1 Wafer Mold Characterization . . . 29
  - 3.2.2 PDMS Master Molds . . . 30
  - 3.2.3 PDMS Master Mold and Microfluidic Structures after Demolding . . . 31
  - 3.2.4 PDMS Microfluidic Structures Derived from Negative Wafer Mold . . . 33
- 3.3 Discussion . . . 34
  - 3.3.1 Wafer Mold Quality and Etching Depth . . . 34
  - 3.3.2 PDMS–PDMS Double Casting and Failure Analyses . . . 34
  - 3.3.3 Direct Demolding from Negative Wafer Mold . . . 35
  - 3.3.4 Advantages and Limitations of Microfabrication . . . 36

4 Conclusion **37**
4.1 Conclusion 37
4.2 Recommendations 38

References **39**

A Microfabrication Flowchart **42**

B Additional Figures **45**
B.1 3D-Printed Structures Under Different Printing Parameters 45
B.2 SEM Images of the 5μm Wafer Mold 48
B.3 Demolding Failure Cases 49
B.4 Aspect Ratio of Wafer Molds 50

C Another Ultimaker Cura Settings **51**

List of Figures

1.1 EU28 and WHO European region DALYs[3] . . . 2
1.2 An example of a microfluidic device for culturing neurons [22] . . . 4
1.3 Schematic illustration of Young's modulus of common materials and tissue [25] . . . 4
1.4 Schematic diagram of SLA and DLP technology [31] . . . 5
1.5 Schematic diagram of DIW [34] . . . 6
1.6 Integration of PDMS axon-guidance microfluidics with MEAs [50, 51] . . . 9

2.1 3D printing experimental setup . . . 12
2.2 Dimensions of the gradient generator (unit: cm) . . . 13
2.3 Dimensions of the microfluidic design (unit: cm) . . . 13
2.4 Viscosity of Inks 10:0, 9:1, 8:2, 7:3, and 0:10 at 25 °C . . . 14
2.5 G' and G" from oscillatory amplitude sweep of Inks 10:0, 9:1, 8:2, 7:3, and 0:10 from 0.001% to 100% strain at 25 °C . . . 15
2.6 Complex viscosity η^*, G' and G'' from frequency sweep of inks 7:3, 8:2 and 9:1 at 25 °C. 17
2.7 Dual-layer extrusion printing of PDMS inks (9:1, 8:2, 7:3) at a constant speed (15 mm/s) and 260 µm nozzle diameter, shown for three displacements: 0.4 mm (top row), 0.7 mm (middle row) and 1.0 mm (bottom row). . . . 18
2.8 Influence of different printing parameters: (A) ink formulation, (B) tip sizes, (C) syringe displacement on the filament widths for 4 printing speeds(5, 10, 15, 20mm/s) . . . 20
2.9 Optical images of 3d printed PDMS structures: (A) microfluidic channels (B) gradient generator . . . 21

3.1 The foil mask layout . . . 25
3.2 Schematic layout of the microfluidic structure for axon guidance . . . 26
3.3 The cell body blocking channels . . . 26
3.4 The flowchart of microfluidic structures fabrication . . . 27
3.5 Optical images of wafer molds: (A)10 µm positive mold, (B)5 µm positive mold, and (C)10 µm negative mold (top to bottom). . . . 29
3.6 Optical images of PDMS master molds: (A) 10µm mold, (B) 5µm mold . . . 30
3.7 SEM images of PDMS master molds: (A) 10µm mold, (B) 5µm mold, (C) measurements 31
3.8 Optical images of PDMS master molds and microfluidic structures after demolding: (A) master molds (B) microfluidic structures . . . 32
3.9 SEM images of PDMS 10µm master mold and microfluidic structures after demolding: (A) master mold (B) microfluidic structures . . . 32
3.10 SEM Images of PDMS structures directly cast from negative wafer mold . . . 33
3.11 Illustration of lateral collapse . . . 35
3.12 Illustration of longitudinal tearing . . . 35

B.1 Ink:9:1, nozzle size:210µm, displacement 0.1mm, printing speed 10mm/s . . . 45
B.2 Ink:8:2, nozzle size:210µm, displacement 0.4mm, printing speed 5mm/s . . . 46
B.3 Ink:8:2, nozzle size:210µm, displacement 0.4mm, printing speed 10mm/s . . . 46
B.4 Ink:8:2, nozzle size:210µm, displacement 0.4mm, printing speed 15mm/s . . . 47
B.5 SEM images of the 5µm wafer mold . . . 48
B.6 Demolding Failure Cases . . . 49
B.7 Cross-sectional view of the 10 µm negative mold cell body blocking channels . . . 50
B.8 Cross-sectional view of the 10 µm positive mold cell body blocking channels . . . 50
B.9 Cross-sectional view of the 5 µm positive mold cell body blocking channels . . . 50

C.1 Another Ultimaker Cura settings . . . 51

List of Tables

2.1 Measured viscosity of PDMS inks at 25 °C (mean, n=3) 14
2.2 Measured G', G'' and yield point from oscillatory amplitude sweep of PDMS inks (0.001%–100% strain, 25 °C; mean, n=3) 16
2.3 Influence of ink formulation and displacement on printed pore perimeter, pore area, and Pr (mean $\pm$ SD; $n = 9$) 19
2.4 Comparison of designed and measured dimensions of 3D-printed PDMS microfluidic structures (mean values, n=5) 21

3.1 Summary of morphological parameters of wafer molds 30

1

Introduction

This chapter outlines the methods for developing microfluidic platforms tailored to neuroscience research. It begins with the global impact and complexity of neurological disorders, highlighting the need for *in vitro* systems that better replicate the neural microenvironment. Polydimethylsiloxane (PDMS)-based platforms are widely used for constructing axon guidance channels due to their mechanical properties, biocompatibility, transparency, and ease of fabrication. To fabricate these devices, two major approaches are discussed: cleanroom microfabrication and additive manufacturing (AM). While AM offers rapid and low-cost prototyping, limited resolution and lack of validation for neuronal culture pose challenges to its application. In contrast, microfabrication can produce high-aspect-ratio (HAR) structures; dense HAR integration remains technically challenging. The chapter concludes by formulating a research question that addresses how to optimize both approaches to create PDMS-based *in vitro* platforms for neuronal applications.

1.1. Background and Significance of Neurological Disorders

Neurological disorders represent a major global health burden, affecting hundreds of millions of people worldwide. These disorders include a broad spectrum of conditions such as Alzheimer's disease, Parkinson's disease, amyotrophic lateral sclerosis, epilepsy, and stroke, many of which are chronic, progressive, and currently incurable [1]. The social and economic impacts are substantial, with increasing prevalence due to global aging populations. For instance, Alzheimer's disease alone affects millions of people globally and is expected to reach 106 million by 2050 [2]. A study on DALYs (disability-adjusted life-years) across the 28 European union (EU) countries and the world health organization (WHO) European region showed that both the total number of DALYs and the DALY rate increase significantly with age [3], indicating a higher disease burden and declining health status in older populations.

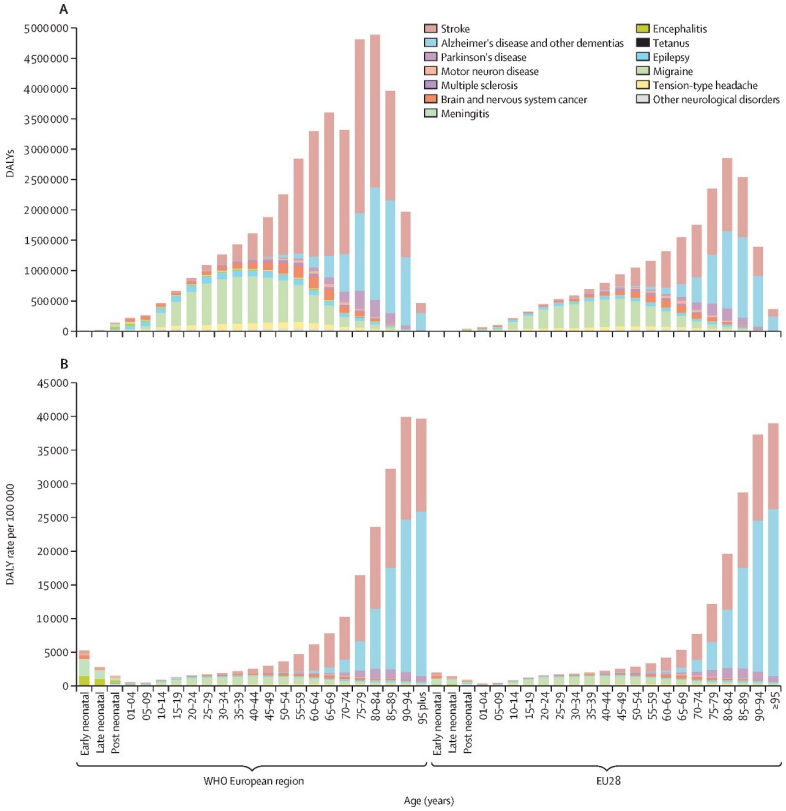

Figure 1.1: EU28 and WHO European region DALYs[3]

1.2. Challenges in Modeling and Treating Neurological Disorders

These disorders often involve complex pathological mechanisms at both cellular and circuit levels, including synaptic dysfunction, neuronal death, glial activation, and circuit reorganization [4]. Despite significant advances in neuroscience, our understanding of the underlying biological processes remains incomplete, and therapeutic options are often limited to symptom management rather than disease modification. One of the major challenges in developing effective therapies is the intricate architecture and functional dynamics of the human nervous system, which complicate the modelling and analysis of disease mechanisms. Many neurological disorders are also highly heterogeneous, with diverse genetic, epigenetic, and environmental contributions, resulting in complex diagnosis and treatment [5]. Therefore, there is an urgent need for advanced experimental systems that allow for the detailed investigation of human neuronal function and dysfunction in both health and disease contexts.

1.3. In Vitro Platforms in Neuroscience

The fundamental units of the human brain are neurons, each of which forms thousands of synaptic connections. These intricate patterns of connectivity enable neurons to assemble into specialized circuits that perform specific functions, thereby making the brain a highly powerful computational system [6]. However, this complexity that poses significant challenges in understanding and treating disorders of the nervous system [7]. Gaining insight into the pathophysiological mechanisms underlying such diseases at the cellular and circuit levels is essential for developing novel and more effective therapeutic strategies. Currently, the approaches to studying brain function include investigating native neural circuits in vivo, ex vivo brain slices, and *in vitro* platforms that mimic in vivo environment [8, 9, 10, 11].

Ideally, the study of the causes of neurological disorders should be conducted using human tissue. However, access to human tissue (typically obtained through autopsy or pathological specimens) is limited, especially in the case of rare diseases [12]. Therefore, suitable model systems are needed to advance our understanding of human nervous system development and disease. Among these, mice and non-human primates are the primary model organisms used in neuroscience research. However, animal models are associated with ethical concerns and are limited by the significant differences be-

tween animal models and human cellular and molecular neurobiology, which restrict our understanding of fundamental mechanisms in the human brain [13]. Ex vivo brain slices offer a compromise, preserving some tissue structure but losing the dynamic functionality of living systems.

1.3.1. Neuron Sources for In Vitro Studies

To study neurons and the nervous system *in vitro*, a reliable source of neurons is essential. Since neurons are post-mitotic and do not undergo cell division, they must be continuously harvested from fresh animals. For decades, rodents have been proven to be an economical, reliable, and valuable source of primary mammalian brain tissue and neuronal cells for most laboratories [14]. Although rodent-based *in vitro* models are feasible, their translational value is clearly limited by interspecies differences. At best, the rodent brain approximates the human central nervous system; however, certain diseases cannot be replicated in rodents at all. The method for generating “induced” pluripotent stem cells (iPSC) was first developed by Shinya Yamanaka’s team [15]. A major advantage of iPSC is that they can be derived postnatally, enabling patient-specific cultures based on individual genetic backgrounds. Moreover, neurons derived from these stem cells are expected to more closely reflect each patient’s unique physiological functions.

1.3.2. Advantages of In Vitro Platforms

In vitro experiments offer a controlled and simplified platform for studying biological processes, making them highly valuable in neuroscience research. By isolating cells or tissues in a laboratory setting, researchers can precisely manipulate experimental conditions, such as chemical gradients [16], mechanical stimulation [17], electrical stimulation [18], or temperature [19], to investigate specific neuronal mechanisms. This controlled environment reduces the uncontrollable variables present in in vivo systems, enhancing experimental reproducibility and facilitating the elucidation of nervous system mechanisms under specific conditions. The second advantage is the significant reduction in labor and resource costs. *In vitro* platforms eliminate the need for complex animal facilities, shorten experimental timelines, and enable high-throughput screening using technologies like microfluidic devices. This helps reduce the cost and time required for bringing drugs to market and supports the development of personalized medical approaches tailored to individual patients and their conditions [20]. These advantages make *in vitro* systems an efficient and ethical choice for treating neurological disorders and advancing our understanding of the nervous system.

1.4. Microfluidic Platforms for Neuronal Research

Conventional cell culture systems, such as two-dimensional monolayer cultures, are widely used to study neuronal growth and differentiation. These systems are simple and cost-effective but often lack complexity and precise spatial control.

In contrast, microfluidics-based cell studies offer significant advantages by enabling precise control over cell positioning and the surrounding microenvironment. This is achieved by using microfluidic structures to either confine or guide cells to designated areas. Additionally, the controlled environment provided by microfluidic platforms helps to mitigate common issues associated with standard *in vitro* techniques, such as unintended external influences, diffusion limitations, and population heterogeneity [21]. Cost-efficiency is another benefit of microfluidic experiments, as the volumes of culture media, hormones, and growth factors required are several orders of magnitude lower than those used in traditional culture flasks.

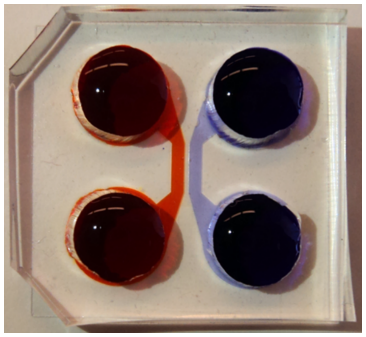

Figure 1.2: An example of a microfluidic device for culturing neurons [22]

1.5. PDMS as an Ideal Material for Microfluidics and Axon Guidance Structures

Common materials used for microfluidic devices include silicon, glass, polymers, thermoplastics, thermosets and paper. Microfluidic devices made from each of these materials play significant roles in their respective research fields. In cell culture studies, polymer-based microfluidic devices have attracted considerable attention. Since polymers were introduced into the microfluidics field, they have remained the materials of choice for commercial applications and high-throughput systems. Among them, PDMS stands out due to its excellent properties. Liquid PDMS prepolymers can be thermally cured at mild temperatures (room temperature to 150 °C) and cast with nanometer resolution from photoresist templates, making the fabrication process easier and more cost-effective compared to silicon or glass molds. Its low surface tension allows the cured PDMS to be easily peeled off from the mold. PDMS chips can form reversible conformal seals with other PDMS layers, glass, or various substrates simply by bringing them into contact. Irreversible bonding to PDMS, glass, or silicon can also be achieved by plasma oxidizing the PDMS surface or using a thin layer of PDMS as an adhesive [23].

Another advantage of PDMS is its high elasticity and low Young's modulus which makes it well-suited for mimicking soft tissues and thus recreating the mechanical environment of cells in vivo. Rachelle et al. [24] reported a PDMS-based substrate material whose elastic modulus can be easily and independently tuned, enabling the simulation of soft tissues across a range spanning three orders of magnitude. They demonstrated that the material supports cell adhesion and growth, and that such substrates can be used to probe the mechanosensitivity of various cellular processes. Compared to glass, silicon, and other rigid materials such as polymethyl methacrylate (PMMA), PDMS is gas-permeable, allowing the exchange of oxygen and carbon dioxide, which is critical for long-term cell culture in sealed microchannels. Due to these properties, PDMS-based devices are widely used in studies involving neuronal cells.

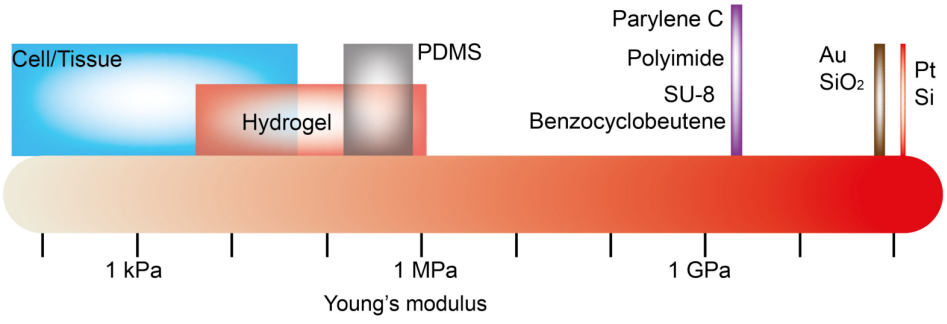

Figure 1.3: Schematic illustration of Young's modulus of common materials and tissue [25]

In neural engineering applications, microfluidic channels are often designed to physically exclude neuronal cell bodies while permitting only thin axons to enter. Such "axon-isolation" structures have been widely used in studies of axonal compartmentalization [26], axonal electrophysiology [27], axon injury and regeneration [28], and synaptic function [29].

Most axon-guidance microfluidic devices are cast in PDMS because it uniquely combines high optical transparency, excellent biocompatibility, and sub-micrometer pattern fidelity. Transparency is especially important: it allows researchers to perform real-time, high-resolution imaging (brightfield, fluorescence, confocal) of growing axons without signal loss or background autofluorescence [30].

By contrast, even though silicon can be etched into equally fine structures, is opaque and unsuitable for live-cell microscopy. Thermoset resists like SU-8 can produce high-aspect-ratio features but tend to be more expensive and less transparent than PDMS. Thermoplastics such as PMMA suffer from poor gas permeability, which hinder oxygen and carbon-dioxide exchange. PDMS's combination of gas permeability, optical clarity, surface-patternability, and low cost therefore makes it the material of choice for axon-guidance platforms.

1.6. Fabrication Methods and Their Challenges for PDMS-based Microfluidics

1.6.1. Additive Manufacturing

There is significant interest in applying AM to the fabrication of microfluidic devices, especially those made from PDMS for biological applications. AM approaches for microfluidic device fabrication can be categorized into two types: indirect printing and direct printing.

In indirect three-dimensional (3D) printing, a sacrificial mold is first printed, and PDMS is then cast over or into the printed structure to replicate the desired microfluidic geometry. After curing, the sacrificial mold is removed, leaving behind a PDMS replica of the internal channel design.

Stereolithography (SLA) and digital light processing (DLP) are two light-based additive manufacturing techniques that are particularly well-suited for producing high-resolution molds from photopolymer resins for indirect PDMS microfluidic fabrication. Their ability to achieve microscale resolution (typically down 50µm) arises from their fundamentally different printing mechanisms compared to extrusion-based techniques.

In SLA printing, a tightly focused UV laser beam is directed by galvanometric mirrors to selectively scan and cure a liquid resin layer according to the desired cross-sectional geometry. The laser spot size, often less than 100µm, and the fine control of the scanning path contribute to high feature resolution.

In contrast, DLP printing cures each layer by projecting a full two-dimensional (2D) image using a digital micromirror device (DMD), which consists of thousands of individually addressable micro-mirrors. Each mirror corresponds to a pixel in the image, allowing precise spatial light modulation. Because DLP cures an entire layer simultaneously, it offers faster printing speeds while maintaining XY resolution typically determined by the pixel pitch of the projection system.

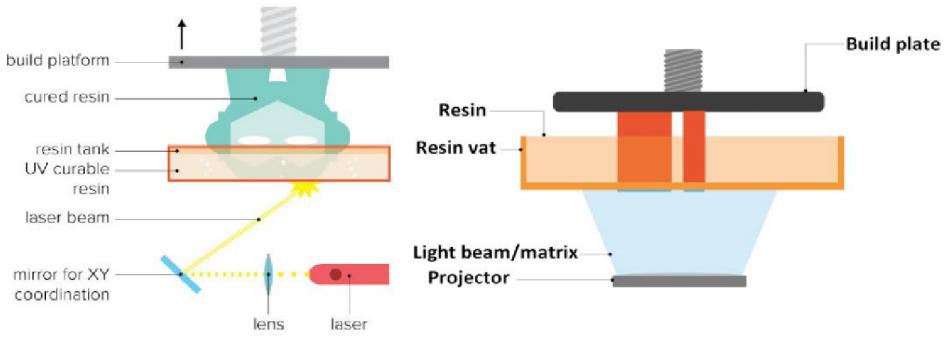

Figure 1.4: Schematic diagram of SLA and DLP technology [31]

The choice of photopolymer resin plays a crucial role in print fidelity and mold usability. Commercial resins such as Formlabs resin and Envisiontec resin are commonly used due to their mechanical stability and ability to replicate fine microchannel geometries. After printing, these resin molds are typically post-cured using UV light to fully polymerize residual monomers and increase hardness. Subsequently, PDMS is cast onto the cured resin mold, cured thermally, and peeled off.

Although SLA and DLP printed resin molds enable fabrication of complex and even 3D interconnected microchannel geometries. These include resin cytotoxicity, and potential inhibition of PDMS

curing at the mold interface if not properly post-processed. Bastien et al. [32] reported that most commercial 3D printing resins inhibit the curing of PDMS. Specifically, photoinitiators in the resin can poison the platinum-based PDMS catalyst, thereby impeding the reliable replication of 3D-printed structures in this elastomeric material. To improve demolding and minimize PDMS curing inhibition, surface treatments such as silanization or extending thermal and UV curing times beyond the commercial formulation recommendations are often applied to the resin mold prior to PDMS casting.

In direct printing of PDMS, direct ink writing (DIW) stands out due to its advantages such as energy efficiency and process simplicity [33]. DIW is an extrusion-based additive manufacturing technique that has emerged as a promising approach for fabricating PDMS-based microfluidic devices without the need for mold. In DIW, a viscoelastic ink is extruded through a fine nozzle under controlled pneumatic or mechanical pressure, allowing programmable deposition of material along predefined 3D paths. This method offers several advantages over indirect printing approaches, including fewer fabrication steps, mold-free prototyping, and the potential to directly construct multilayer.

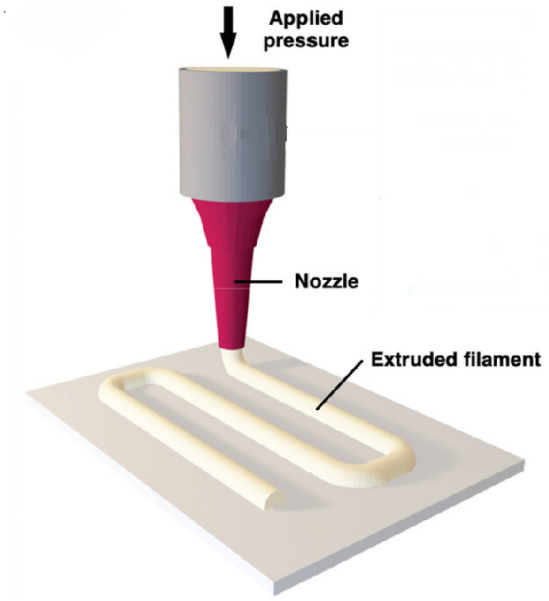

Figure 1.5: Schematic diagram of DIW [34]

However, printing PDMS via DIW presents considerable challenges due to the inherent rheological properties of standard PDMS prepolymers, such as Sylgard 184. These formulations are low-viscosity liquids before curing, making them unsuitable for extrusion-based printing in their native state. To overcome this limitation, recent studies have focused on formulating printable PDMS inks with shear-thinning behavior and shape retention upon deposition. A common strategy is to mix low-viscosity commercial Sylgard 184 PDMS with rheological modifiers, such as PDMS SE 1700, graphene oxide, or carbon nanotubes, to increase viscosity and yield stress [35, 36, 37]. Other approaches include heat-assisted PDMS curing [38] and the use of UV-curable PDMS for printing [39].

DIW offers a mold-free alternative for fabricating PDMS-based structures. While there has been notable progress in formulating printable PDMS inks and characterizing their line widths, aspect ratios, or integration with stretchable electronics and sensors [40, 41], the direct application of DIW-printed PDMS microchannels in cell culture, particularly for neurons, remains underexplored. There is currently a lack of comprehensive studies validating the biocompatibility, long-term stability, and neuronal support capacity of such printed platforms, which are critical for neuroscience applications. This gap limits the impact of DIW in neuronal system development.

1.6.2. Microfabrication

Despite the rapid progress in 3D printing technologies, their limited resolution continues to pose a major constraint in fabricating microfluidic devices for neuroscience applications. Most conventional 3D printers lack the ability to produce cellular or subcellular-scale features, which are essential for isolating

fine neuronal structures such as axons and dendrites. This resolution limits the utility of 3D-printed platforms in studies that require high-precision microenvironments, such as axon guidance, localized stimulation, or axon–soma compartmentalization. In *in vitro* neuroscience research, the ability to isolate and control distinct compartments of a neuron, such as the soma, axon, and dendrites, is essential for dissecting neuronal function, connectivity, and response to external stimuli. One of the landmark approaches in this area was introduced by Taylor et al. [26], who developed a microfluidic device featuring parallel microgrooves (approximately 10µm wide and 3µm high) that physically restrict cell bodies while allowing axons to grow across compartments. This architecture enabled the physical and fluidic isolation of axons from their somas, opening new possibilities for investigating axonal transport, degeneration, and regeneration in a controlled environment. Since then, similar microgroove-based designs have been widely adopted as the standard for compartmentalized neuronal cultures, especially in studies of axon guidance, axon-specific stimulation, and neuromuscular junction [42, 43].

Fabricating the precise microstructures necessary for neuronal research often requires advanced microfabrication techniques, including photolithography, wet etching, dry etching, as well as focused ion beam (FIB) milling and electron beam lithography. Many of these processes utilize silicon wafers as substrates, owing to their superior rigidity, dimensional stability, and excellent wear resistance, enabling the accurate replication of micro and nanoscale features [44].

However, despite their precision and widespread use, most microfluidic devices fabricated through traditional cleanroom microfabrication methods remain inherently 2D, limiting the ability to replicate the 3D microenvironment found in vivo. Neural tissues in the brain and spinal cord are embedded in a highly organized 3D extracellular matrix, where neurons are subject to topographical, mechanical, and biochemical cues in all spatial dimensions. An ideal 3D *in vitro* model not only incorporates appropriate cell types and biomimetic extracellular matrix (ECM), but also provides biochemical cues (e.g., growth factors) and biophysical signals (e.g., mechanical stimulation). This ensures greater precision and reliability in recapitulating the complex microenvironment encountered in native tissues. These extracellular cues can significantly influence cell viability, proliferation, migration, and differentiation within the brain and spinal cord [45]. Therefore, mimicking 3D geometries in microfluidic neural platforms is essential for achieving physiologically relevant outcomes.

This is where HAR structures offer a promising design feature. By extending vertically while maintaining narrow lateral dimensions, these structures facilitate multilayer stacking and the formation of 3D deformable channels [46]. They can be used for cell separation [43] and are particularly suited for constructing axon guidance pathways or axon channels, in which axons are also allowed to extend vertically through the structures, while cell bodies remain restricted due to size exclusion. This is meaningful for studying the 3D growth behavior of axons.

Photolithography and deep reactive ion etching (DRIE) are two predominant microfabrication techniques used to create HAR structures. Many of these processes use silicon wafers as substrates due to their excellent dimensional stability and wear resistance [44]. The process typically begins with the design of a microfluidic pattern using computer-aided design (CAD) software, followed by the creation of a master mold using photolithography. In this process, a silicon wafer is coated with a photoresist, exposed to ultraviolet (UV) light through a patterned mask, and developed to create a mold with precise microchannels. This mold can be either negative or positive. Positive molds are commonly made using SU-8. SU-8 enables the fabrication of structures with thicknesses exceeding 1mm and aspect ratios up to approximately 40:1 [47]. Photolithography can be performed using standard contact UV exposure systems operating at wavelengths between 320 and 450nm. The developed SU-8 structures generally exhibit smooth surfaces. The simplicity of this method and its compatibility with standard cleanroom environments are key advantages of the SU-8 UV process [44]. After fabrication, these molds are typically used to cast PDMS replicas.

Alternatively, negative molds can be fabricated using DRIE, a powerful technique widely adopted in MEMS and microfluidic device fabrication. DRIE allows for the creation of deep, vertical structures in silicon substrates with high aspect ratios and excellent sidewall definition. Among various DRIE approaches, the Bosch process is the most used. It operates by alternating cycles of SF_6-based isotropic etching and C_4F_8-based passivation, which together enable anisotropic etching with minimal lateral undercutting [48]. This makes it ideal for producing precise, narrow channels that are well-suited for microfluidic applications requiring cellular-level resolution. In contrast to SU-8 photoresist molds, which suffer from mechanical degradation after repeated PDMS demolding [49], DRIE-etched silicon molds exhibit exceptional mechanical robustness and can be reused multiple replication cycles without di-

mensional deformation. This durability, combined with their ability to produce complex HAR features, makes DRIE attractive for neuronal applications such as axon guidance platforms.

Nevertheless, despite the established capabilities of photolithography and DRIE in fabricating HAR structures, significant challenges persist in achieving both HAR and high-density microchannel arrays simultaneously. Reports demonstrating the successful fabrication of densely packed HAR structures remain scarce due to mechanical instabilities, such as channel collapse or deformation during fabrication and demolding. Yet, achieving dense arrays of HAR channels would substantially increase experimental throughput, enabling multiplexed analyses of neuronal responses under varied chemical and physical conditions. Moreover, high-density structures have potential advantages in constructing more complex and realistic neural networks that closely approximate the dense neuronal connectivity observed in vivo. It is therefore important to address these fabrication challenges in advancing *in vitro*neuronal models towards true three-dimensional complexity and physiological relevance.

1.7. Integration of PDMS Axon-Guidance Structures with Microelectrode Arrays (MEAs)

Microelectrode arrays (MEAs) are *in vitro* platforms consisting of a grid of closely spaced, extracellular microelectrodes embedded in a rigid substrate. These electrodes can simultaneously record electrical spiking and local field potentials from multiple neurons or deliver precise electrical stimulation to targeted cell populations. When combined with PDMS-based axon-guidance microchannels, MEAs exhibit powerful new capabilities: (1) physical isolation of axons into predefined paths for determined signal routing, and (2) spatially resolved stimulation and recording along those paths, enabling high-resolution electrical measurements of neural network dynamics. In one study, Léo et al. [50] created an implantable biohybrid neural construct composed of neuronal spheroids housed in separate chambers, all interconnected by PDMS microstructures and positioned on high-density MEAs. By patterning dendritic guidance channels directly over the electrode arrays, each spheroid could be stimulated and recorded independently, without electrical crosstalk from neighboring units. This configuration achieved sub-100 µm resolution in both stimulation and recording, demonstrating the potential to target deep-brain analogues for applications such as restoring visual function in blind patients.

Additionally, Katarina et al. [51] designed a radial array of PDMS microchannels—ranging from 1.5 to 75 µm in width—emanating from a 400 µm-diameter central well placed over an MEA. After seeding neuronal spheroids containing roughly 500 cells, axons entered each channel uniformly, and high-throughput electrical recordings tracked their outgrowth dynamics. Axonal extension peaked in the second week of culture—reaching up to 2 mm in channels wider than 2.8 µm—before stabilizing, while narrower channels limited growth to under 1 mm. By varying the number of channels, the researchers modulated axon bundle size and observed that bundles containing more axons extended further and exhibited distinct conduction velocities and synchrony patterns. This integration of PDMS guidance structures with MEAs provides a powerful platform for dissecting axon physiology, modelling injury and regeneration, and engineering bespoke neural networks.

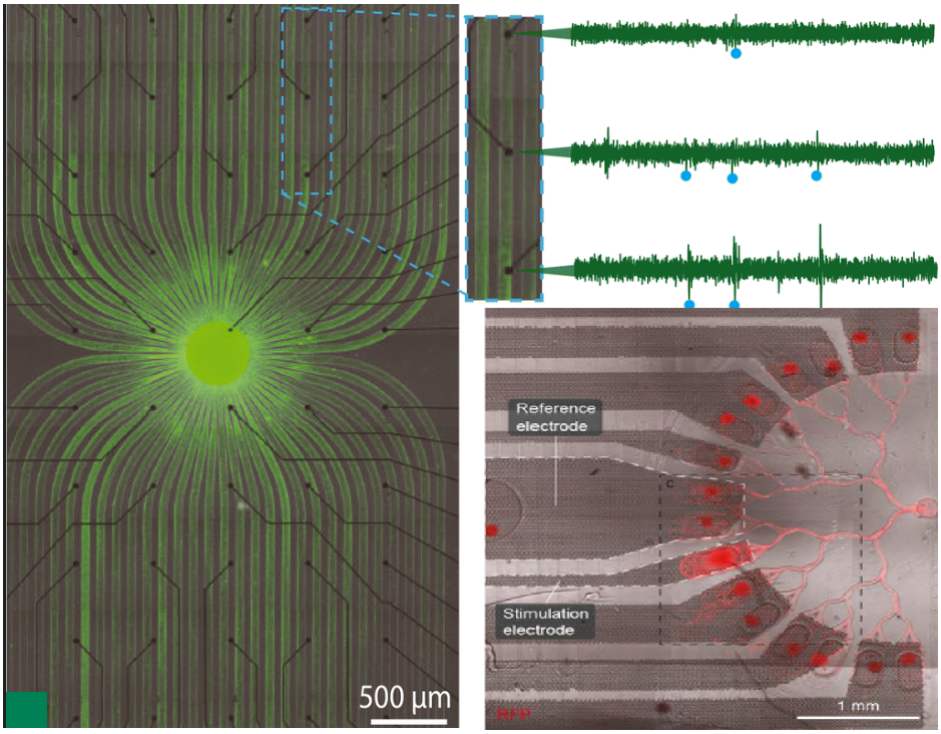

Figure 1.6: Integration of PDMS axon-guidance microfluidics with MEAs [50, 51]

1.8. Research Question

The current literature suggests a significant gap in the development of microfluidic platforms that effectively replicate 3D microenvironments suitable for *in vitro* neuroscience research. While a number of compartmentalized 2D microfluidic systems have been proposed to study neuronal growth, axonal guidance, and cell–cell interactions, these designs remain inherently limited in their ability to mimic the vertical complexity, hierarchical organization, and structural density that characterize the in vivo nervous system. In particular, 2D layouts can capture lateral compartmentalization but fail to reconstruct critical aspects such as layered tissue architectures, depth-dependent gradients, and the extracellular matrix that modulates neural connectivity in the brain.

Cleanroom microfabrication techniques, such as SU-8 photolithography, reactive ion etching (RIE), and DRIE, have provided powerful routes to achieve HAR microstructures that could better capture the spatial constraints of neuronal networks. These methods offer submicron resolution, excellent reproducibility, and compatibility with established microelectronic integration processes. However, despite these advantages, relatively few studies have succeeded in producing dense HAR arrays specifically tailored for neural applications. This limitation is largely attributed to challenges including photoresist stability during multi-step fabrication, mechanical fragility of tall and narrow structures, and non-uniform etching across large wafer areas. Such constraints often result in device failure during demolding, reduced yield, or compromised biocompatibility of the final structures.

Meanwhile, additive manufacturing approaches, particularly DIW, have emerged as highly attractive alternatives due to their flexibility, low cost, and ability to rapidly iterate device designs without the need for cleanroom infrastructure. DIW has demonstrated great potential in fabricating PDMS-based devices with tunable mechanical properties, enabling the creation of curved geometries, gradient structures, and soft interfaces that more closely resemble the neural tissue microenvironment. Nevertheless, most existing studies remain focused on embedding electronic and chemical sensors into PDMS substrates. There is a lack of systematic validation regarding the long-term biocompatibility, microchannel stability, and the ability of DIW-fabricated PDMS platforms to support physiologically relevant neural network formation, particularly when used for microfluidic structures and axon guidance.

The resulting research question based on this identified gap is formulated as:

"How can additive manufacturing and photolithography technologies be optimized to produce high-aspect-ratio and high-density microstructures for axon guidance?"

This system could serve as a tool for studying neuronal development, axon guidance, neural connectivity in 3D environments. Multiple sub-objectives will be answered to achieve this goal:

- To formulate and characterize DIW PDMS inks with appropriate rheological properties and printability.
- To design, fabricate and characterize DIW PDMS structures.
- To explore the microfabrication limits in producing dense HAR microchannels suitable for axon-guidance applications.

2

Direct Ink Writing of PDMS Structures

2.1. Materials and Methods

2.1.1. Ink Preparation

The viscoelastic PDMS inks were formulated by blending two types of silicone elastomers: a shear-thinning PDMS material, SE 1700 (Dow Corning, Japan), and a low-viscosity PDMS material, Sylgard 184 (Dow Corning, USA), which was used to dilute SE 1700 to achieve the desired rheological properties.

Prior to blending, both SE 1700 and Sylgard 184 base components were mixed with their respective curing agents at a weight ratio of 10:1 (base:curing agent) in a mixer (Speedmixer DAC 150.1 FVZ). The two mixtures were then degassed separately in a vacuum desiccator (Lab Commpanion) for 15 minutes. The final inks were loaded into 20mL syringes (Fisher scientific, China) at room temperature. The total weight of each filled syringe was measured, and an object of equal weight was placed on the opposite side of the centrifuge (Eppendorf Centrifuge 5702) for balance. The syringes were then centrifuged at 3,000rpm for 2 minutes to remove all air bubbles and to drive the ink toward the end. Finally, PDMS inks were prepared by blending SE 1700 and Sylgard 184 in five different weight ratios: 10:0, 9:1, 8:2, 7:3, and 0:10.

2.1.2. Rheological Characterization

Rheological measurements were performed using a HAAKE MARS III rheometer (Thermo Scientific) equipped with a parallel plate geometry (20mm diameter). An appropriate amount of the prepared PDMS ink was dispensed onto the bottom plate, and the upper plate was adjusted to ensure that the ink fully occupied the gap between the two plates. After zeroing the normal force, rheological measurements were initiated. The storage modulus (G′) and loss modulus (G″) were recorded during amplitude sweeps performed at a constant frequency of 1Hz over a strain range of 0.001% to 100%, for ink formulations with SE 1700: Sylgard 184 weight ratios of 10:0, 9:1, 8:2, 7:3, and 0:10. The 10:0 and 0:10 formulations were used as control groups. In addition, frequency sweeps were conducted to obtain G′, G″, and complex viscosity (|η*|) at a constant strain of 0.01%, within the linear viscoelastic regime, over a frequency range of 100 to 0.1Hz. Flow and viscosity curves were obtained through rotational tests, with shear rates ranging from 0.01 to 1000s-1. All measurements were performed at a controlled temperature of 25°C. After each measurement set, the parallel plates were carefully cleaned with isopropanol (IPA), and the procedure was repeated for the next sample.

2.1.3. Printability Analysis

The model used for printability testing was designed using CAD software (SOLIDWORKS 2023 SP2.1). 3D printing was performed using a commercial desktop printer (Ultimaker 2+) that was modified by replacing the original print head with a custom-made ink extrusion system consisting of a 25mL syringe holder and a mechanically driven syringe pump [52]. PDMS ink was loaded into the syringe barrel at room temperature and capped with dispensing nozzles of 25GA (260µm), 27GA (210µm), and 30GA (160µm) (PATIKIL beveled tip dispenser, China).

The syringe pump controls the displacement of the syringe plunger. Since the ink is extruded

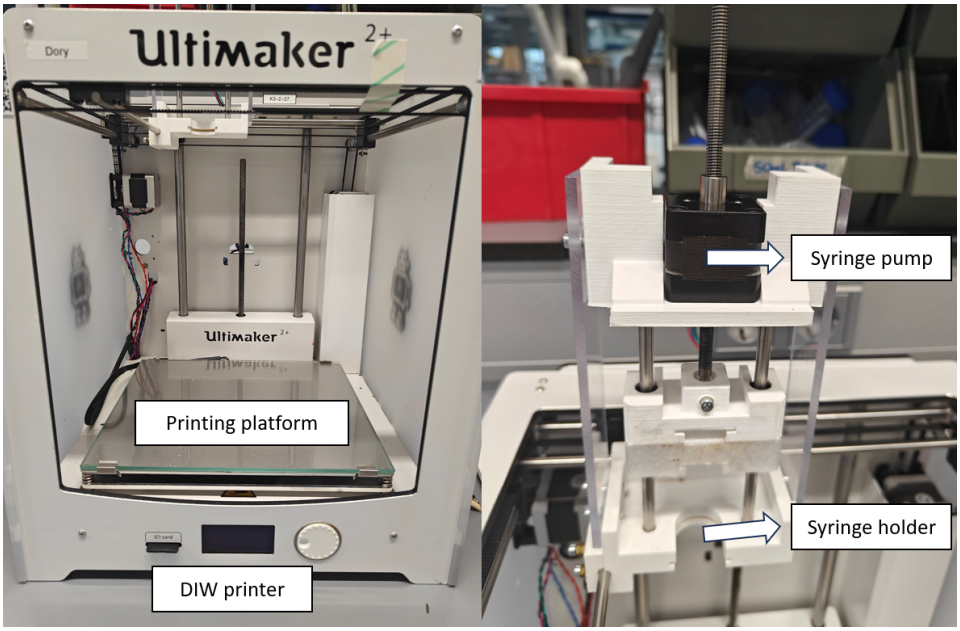

Figure 2.1: 3D printing experimental setup

slowly during printing and the extruded volume typically exceeds the amount required for deposition, extrusion pressure can be represented by displacement. The printing speed and paths were controlled using UltiMaker Cura 5.9.1. Dual-layer printing tests were performed under a constant printing speed (15mm/s) and a fixed nozzle diameter (260um) with three different ink formulation (9:1, 8:2 and 7:3) at three displacements (0.4mm, 0.7mm and 1mm). The purpose of this experiment was to evaluate the basic printability of prepared PDMS ink and to preliminarily assess the influence of nozzle diameter and printing speed on the printing quality. In the printed two-layer structures, the spacing between adjacent filaments was kept constant in both the x and y directions. Veli et al. [35] use circularity (C) to define printability (Pr):

$$C = \frac{4\pi A}{L^2} \tag{2.1}$$

where L and A represent the perimeter and area of the pore, respectively. A C value of 1 indicates that the enclosed area is closest in shape to a perfect circle. Since the maximum circularity of a square is equal to π/4, the Pr of the ink based on the printed square shape is defined as follows:

$$Pr = \frac{\pi}{4C} = \frac{L^2}{16A} \tag{2.2}$$

This indicates that when the printed pore approximates a perfect square, a Pr value of 1 reflects optimal printability of the ink under the given conditions. The greater the deviation from 1, the poorer the printability. To evaluate different parameters influencing the printability, the printed filament widths were measured and analyzed under different conditions, including three types of inks (9:1, 8:2, and 7:3), three nozzle sizes (260, 210, and 160 µm), three levels of displacement (0.1 mm, 0.4 mm, 0.7 mm), and four printing speeds (5, 10, 15, and 20 mm/s). In all experiments, the gap between the nozzle tip and the printing platform was fixed at 0.2 mm. After printing, the samples were cured by heating at 100°C for 30 minutes in a VacuTherm Vacuum Oven (Thermo Scientific). The filament widths were measured using a Dino-Lite microscope.

2.1.4. 3D Printing of Microfluidics

A gradient generator for producing solute concentration gradients and a simplified open-channel microfluidic design, were modeled using SolidWorks. Both designs are of single-layer structures. The corresponding printing paths were automatically generated by UltiMaker Cura. 3D models were printed using ink 8:2 and a 210 µm nozzle tip, with a constant printing speed of 10 mm/s and a syringe dis-

placement of 0.1 mm.

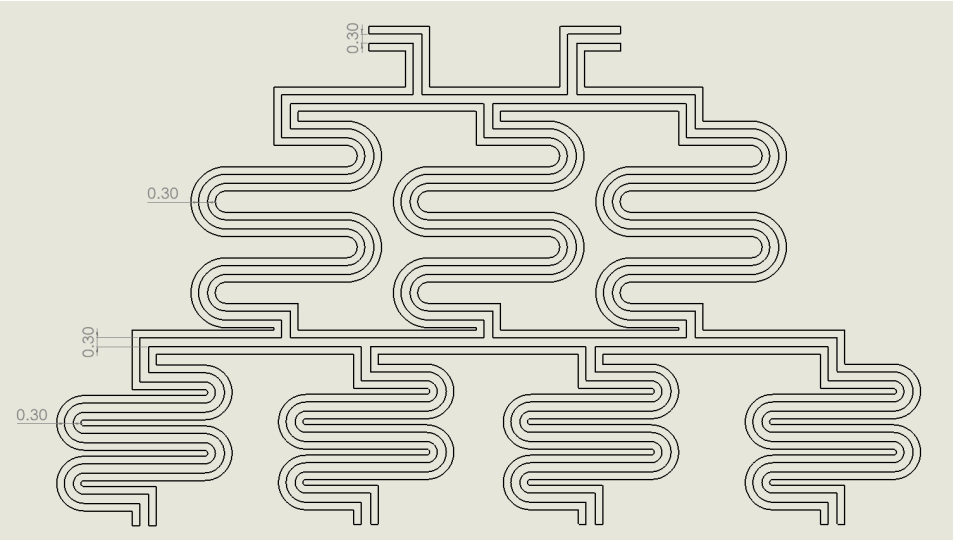

Figure 2.2: Dimensions of the gradient generator (unit: cm)

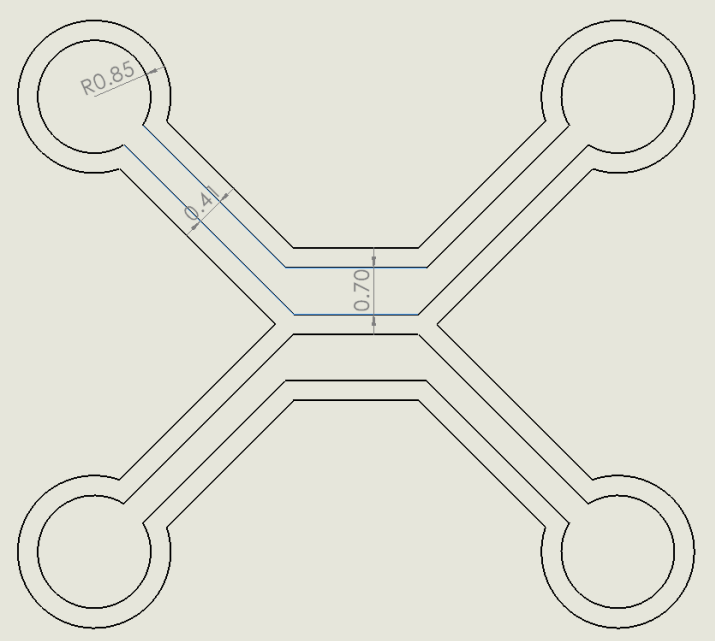

Figure 2.3: Dimensions of the microfluidic design (unit: cm)

2.2. Results

2.2.1. Rheological Properties

The flow and viscoelastic behavior of the five PDMS ink formulations (0:10, 9:1, 8:2, 7:3 and 10:0) were characterized by shear viscosity, oscillatory amplitude sweep and oscillatory frequency sweep tests.

Shear Viscosity Test

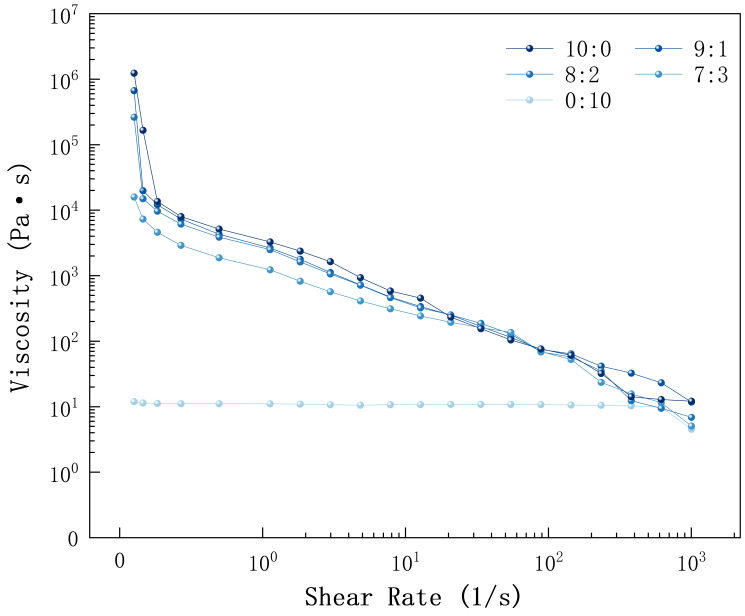

Figure 2.4: Viscosity of Inks 10:0, 9:1, 8:2, 7:3, and 0:10 at 25 °C

Table 2.1: Measured viscosity of PDMS inks at 25 °C (mean, n=3)

Shear rate (s^{-1})	**Viscosity** (Pa·s)				
	0:10	**9:1**	**8:2**	**7:3**	**10:0**
0.1	12.1	667,100.3	263,100.2	15,950.4	1,237,000.0
1.0	11.1	2,654.4	2,503.0	1,234.5	3,290.0
10.0	10.8	338.5	323.4	287.3	502.3
100.0	10.7	68.4	63.2	60.3	69.3
1,000.0	4.5	11.8	6.9	5.1	12.1

All viscosity values represent mean measurements of three replicates at 25 °C. The PDMS SE1700–Sylgard blends (10:0, 9:1, 8:2, and 7:3) each displayed shear-thinning behavior, with viscosities that dropped steeply from the lowest shear rate (0.1 s^{-1}) through around 10 s^{-1} and then declined more gradually up to 1000 s^{-1}. At 0.1 s^{-1}, the pure SE1700 formulation (10:0) exhibited the highest viscosity on the order of 106 Pa·s, while the 9:1, 8:2, and 7:3 blends measured approximately 6.7 × 10^5, 2.6 × 10^5, and 1.6 × 10^4Pa·s, respectively. By 100 s^{-1}, these shear-thinning inks had converged to viscosities of order 10^1Pa·s (roughly 60–70 Pa·s), and at 1000 s^{-1} they reached values below about 15 Pa·s. In contrast, the pure Sylgard formulation (0:10) behaved as a newtonian fluid, maintaining a nearly constant viscosity of 12 ± 1 Pa·s across the entire shear-rate range (Figure 2.4, Table 2.1).

Oscillatory Amplitude Sweep Test

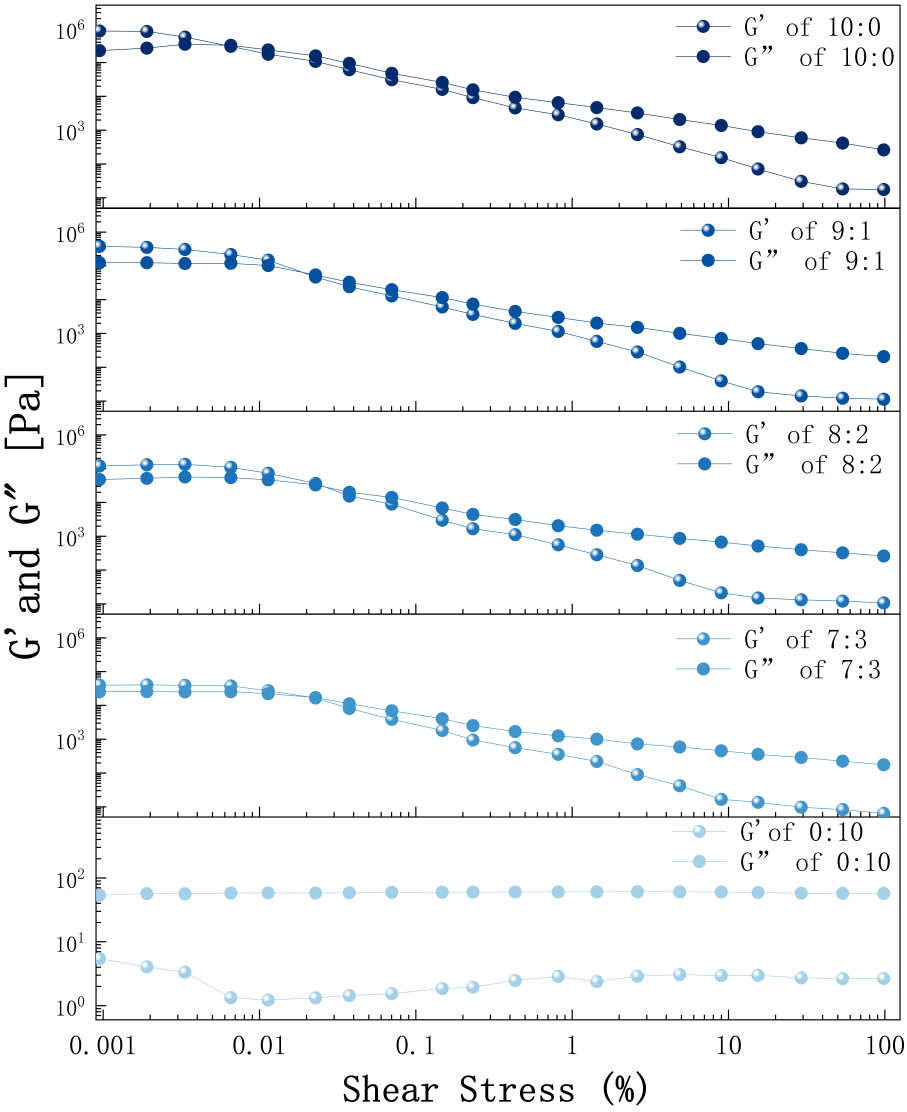

Figure 2.5: G' and G" from oscillatory amplitude sweep of Inks 10:0, 9:1, 8:2, 7:3, and 0:10 from 0.001% to 100% strain at 25 °C

Table 2.2: Measured G', G'' and yield point from oscillatory amplitude sweep of PDMS inks (0.001%–100% strain, 25 °C; mean, n=3)

Formulation	0.001%		0.01%		0.1%		Yield point
	G' (Pa)	G'' (Pa)	G' (Pa)	G'' (Pa)	G' (Pa)	G'' (Pa)	
0:10	5.4	53.8	1.2	58.3	1.8	60.0	NA
9:1	379,515.8	123,990.8	147,689.9	101,981.9	9,491.2	15,705.5	0.01 % to 0.02 %
8:2	120,482.0	47,725.3	73,261.4	46,796.4	5,962.5	10,500.0	0.02 % to 0.04 %
7:3	39,665.5	25,602.0	27,401.6	22,412.3	2,852.3	5,507.1	0.02 % to 0.04 %
10:0	860,417.2	226,912.5	177,829.3	238,676.5	23,628.5	37,193.2	0.003 % to 0.007 %

Ratios denote SE1700:Sylgard 184 by weight; G'/G'' in Pa. Yield point is the strain where $G' = G''$.

All oscillatory amplitude sweep measurements were conducted at 25 °C with three replicates per formulation. The storage modulus G' exceeded the loss modulus G" at very low strain (0.001%) for PDMS SE1700–Sylgard blends (10:0, 9:1, 8:2, and 7:3). As strain increased from 0.001% to 100%, both G' and G" decreased steadily for these blends, and a crossover point was observed in each case. In contrast, the pure Sylgard formulation (0:10) showed a fluid-like response at all strains, with G" remaining above G' and no crossover within the tested strain range (Figure 2.5).

From Table 2.2, the initial moduli at 0.001 % strain for the blends spanned from 3.97×10^4 Pa (7:3) to 8.60×10^5 Pa (10:0) for G' and from 2.56×10^4 Pa to 2.27×10^5 Pa for G". At 0.01% strain, G' values fell to between 1.48×10^5 Pa (9:1) and 2.74×10^4 Pa (7:3), and at 0.1% strain they further decreased to 9.49×10^3 Pa, 5.96×10^3 Pa, 2.85×10^3 Pa, and 2.36×10^4 Pa for the 9:1, 8:2, 7:3, and 10:0 inks, respectively. Corresponding G" values at 0.1% strain ranged from 1.57×10^4 Pa down to 60 Pa (0:10). The yield points, defined by the strain at which G′ and G″ cross, occurred at approximately 0.003%-0.007% for the 10:0 ink, 0.01%-0.02% for 9:1, and 0.02%-0.04% for both the 8:2 and 7:3 blends. Pure Sylgard (0:10) did not reach a yield point within the tested strain range.

Oscillatory Frequency Sweep Test

All oscillatory frequency sweep tests were conducted at 25°C. At all frequencies, the G' of PDMS SE1700–Sylgard blends at various ratios was higher than the G". Specifically, for the 7:3 ink, as the frequency increased from 0.1Hz to 100Hz, G' rose from 3.50×10^4 to 1.80×10^5Pa, G" increased from 2.96×10^4 to 1.66×10^5Pa, and the complex viscosity (η*) decreased from 7.3×10^4 to 392Pa·s. For the 8:2 ink, G' rose from 4.3×10^4 to 2.33×10^5Pa, G" increased from 3.9×10^4 to 2.20×10^5Pa, and η* decreased from 9.3×10^4 to 511Pa·s. For the 9:1 ink, G′ rose from 5.44×10^4 to 3.07×10^5Pa, G" increased from 4.14×10^4 to 1.83×10^5Pa, and η* decreased from 1.09×10^5 to 570Pa·s.

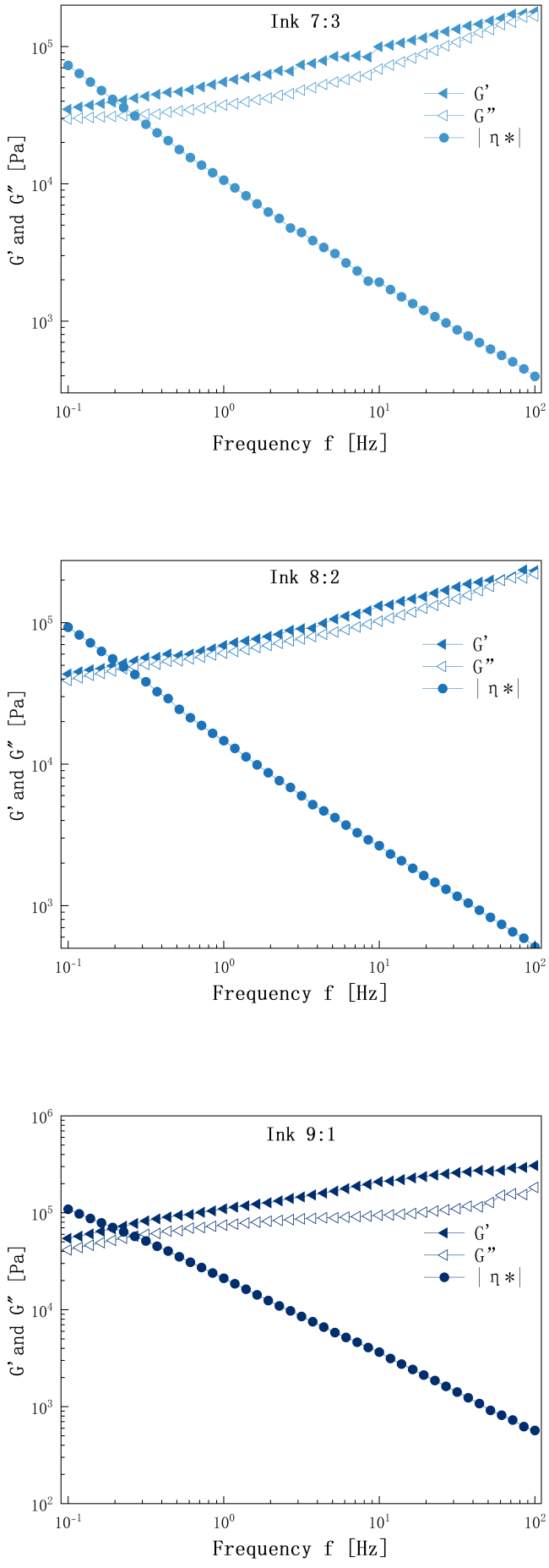

Figure 2.6: Complex viscosity η^*, G' and G'' from frequency sweep of inks 7:3, 8:2 and 9:1 at 25 °C.

2.2.2. PDMS Printability

Based on the above results, the 0:10 PDMS ink does not exhibit shear-thinning behavior and consistently behaves as a liquid; therefore, it is not printable. In contrast, the 10:0 ink is extremely difficult to extrude through small nozzles, while extrusion through larger nozzles defeats the purpose of achieving high-resolution printing. Consequently, it is not discussed further in this section. The printability characterization in this section focuses solely on the 9:1, 8:2, and 7:3 inks.

Dual-layer printing

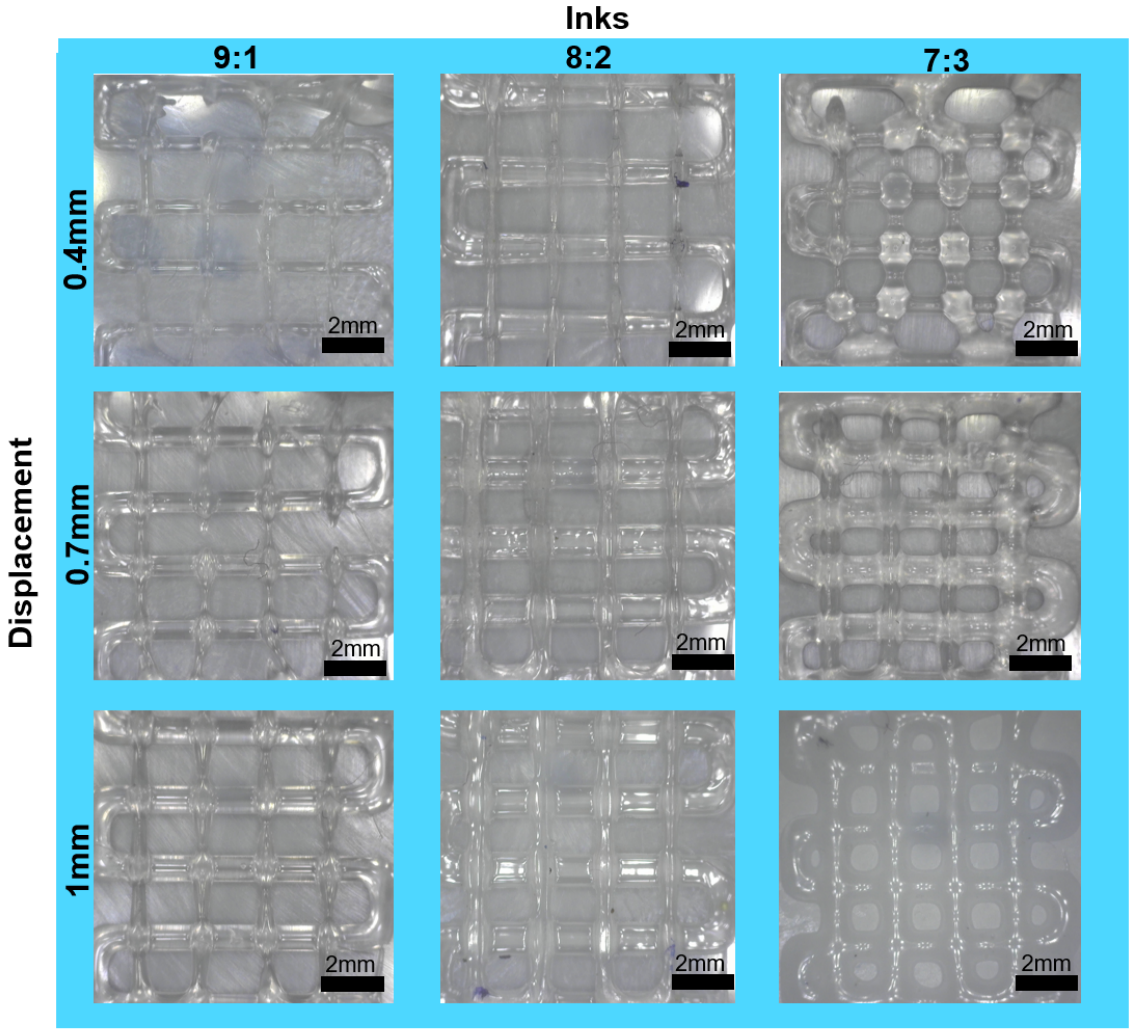

Figure 2.7: Dual-layer extrusion printing of PDMS inks (9:1, 8:2, 7:3) at a constant speed (15 mm/s) and 260 µm nozzle diameter, shown for three displacements: 0.4 mm (top row), 0.7 mm (middle row) and 1.0 mm (bottom row).

All measurements were based on nine replicates (n = 9). For the 9:1 ink formulation, no stable pore structures were detected at displacements of 0.4 mm and 0.7 mm. At a displacement of 1.0 mm, the mean perimeter was 5.39 ± 0.80 mm, the mean pore area was 1.99 ± 0.06 mm², and the Pr value was 0.91 ± 0.02.

For the 8:2 ink formulation, increasing the displacement from 0.4 mm to 1.0 mm produced a decrease of the pore area. At 1.0 mm, the mean perimeter measured 4.76 ± 0.24 mm, the mean pore area was 1.55 ± 0.12 mm², and Pr was 0.91 ± 0.03. At 0.7 mm, the mean perimeter increased to 5.14 ± 0.20 mm, the pore area to 1.72 ± 0.12 mm², and Pr to 0.96 ± 0.02. At 0.4 mm, the perimeter reached 5.96 ± 0.17 mm, the area 2.30 ± 0.13 mm², and Pr remained at 0.96 ± 0.01.

For the 7:3 ink formulation, a displacement of 0.4 mm yielded a mean perimeter of 4.80 ± 0.20 mm, a mean pore area of 1.71 ± 0.12 mm², and a Pr value of 0.84 ± 0.01. At 0.7 mm, the mean perimeter

Table 2.3: Influence of ink formulation and displacement on printed pore perimeter, pore area, and Pr (mean $\pm$ SD; $n = 9$)

Ink formulation	Displacement (mm)	Perimeter (mm)	Pore area (mm^2)	Pr
9:1	0.4	NA	NA	NA
	0.7	NA	NA	NA
	1.0	5.39 ± 0.80	1.99 ± 0.06	0.91 ± 0.02
8:2	0.4	5.96 ± 0.17	2.30 ± 0.13	0.96 ± 0.01
	0.7	5.14 ± 0.20	1.72 ± 0.12	0.96 ± 0.02
	1.0	4.76 ± 0.24	1.55 ± 0.12	0.91 ± 0.03
7:3	0.4	4.80 ± 0.20	1.71 ± 0.12	0.84 ± 0.01
	0.7	4.35 ± 0.11	1.31 ± 0.07	0.90 ± 0.02
	1.0	3.34 ± 0.12	0.82 ± 0.04	0.80 ± 0.02

NA: no stable pores formed.

decreased to 4.35 ± 0.11 mm, the pore area to 1.31 ± 0.07 mm², and Pr rose to 0.90 ± 0.02. At 1.0 mm, the perimeter further decreased to 3.34 ± 0.12 mm, the pore area to 0.82 ± 0.04 mm², and Pr was 0.85 ± 0.02.

Filament widths measurements

Filament width measurements were conducted under four different printing speeds (5, 10, 15, 20mm/s), various ink formulations (9:1, 8:2, 7:3), different tip sizes (260µm, 210µm, 160µm), and different displacements (0.1mm, 0.4mm, 0.7mm), as shown in Figure 2.8. Missing data points in the figure indicate that the ink was not printable under the corresponding conditions.

In Figure (A), with the displacement fixed at 0.4mm, the extrusion filament widths of different ink formulations were compared under identical conditions. As the proportion of SE1700 in the ink increased, the extruded filament widths decreased. Meanwhile, with a smaller nozzle size and higher printing speed, inks with a higher SE1700 content became increasingly difficult to extrude.

In Figure (B), with the displacement fixed at 0.4mm, all three inks showed a decrease in filament width when the nozzle size was reduced from 260µm to 210µm. However, when the nozzle size was further reduced to 160µm, the filament widths of inks 8:2 and 7:3 increased instead, whereas ink 9:1 became difficult to extrude at all printing speeds.

Figure (C) investigates the effect of displacement on filament width. It can be observed that for all ink formulations, filament width decreases as the displacement decreases. Moreover, smaller displacements can only produce printable filaments at lower printing speeds.

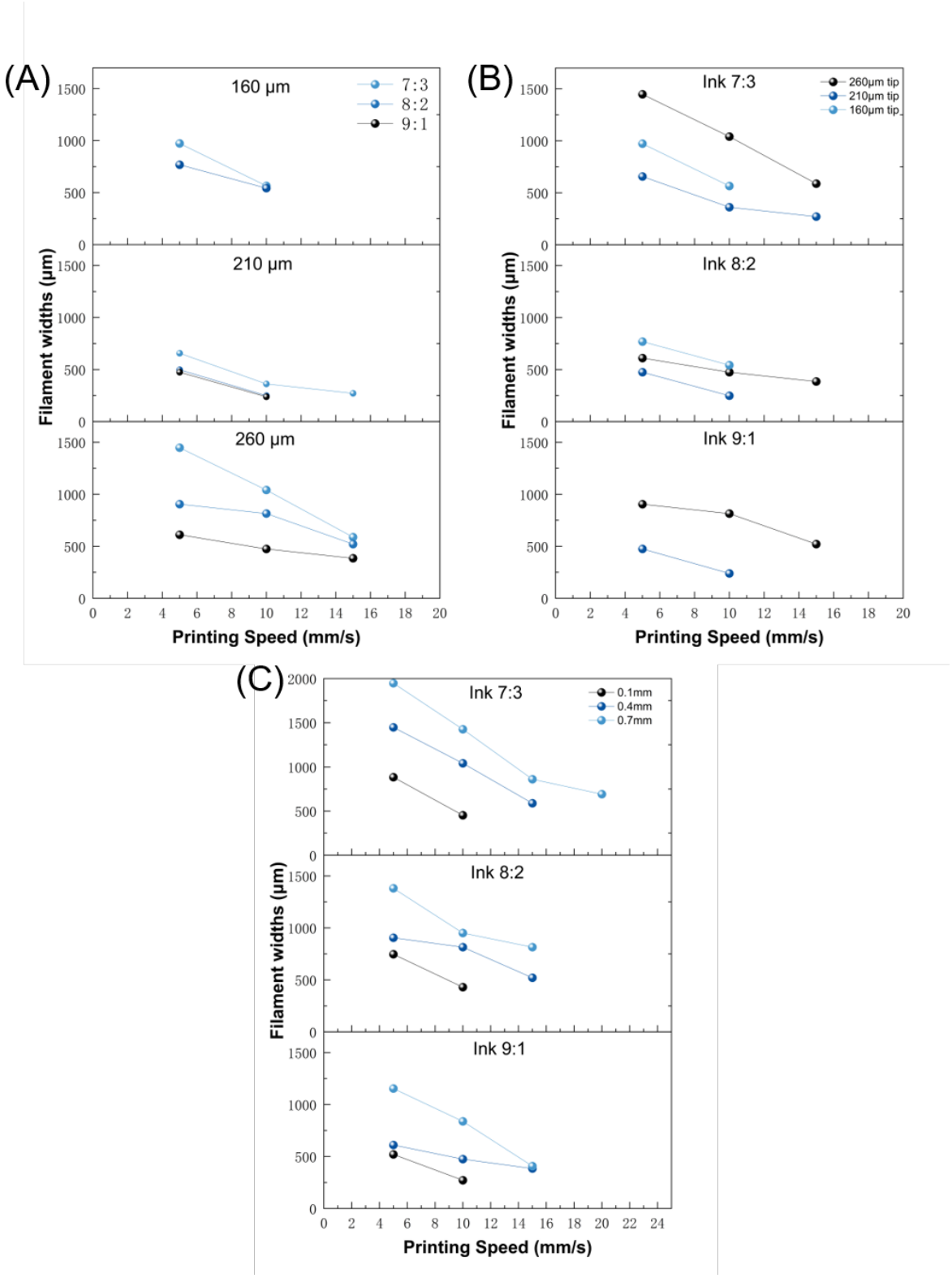

Figure 2.8: Influence of different printing parameters: (A) ink formulation, (B) tip sizes, (C) syringe displacement on the filament widths for 4 printing speeds(5, 10, 15, 20mm/s)

3D printed models measurements

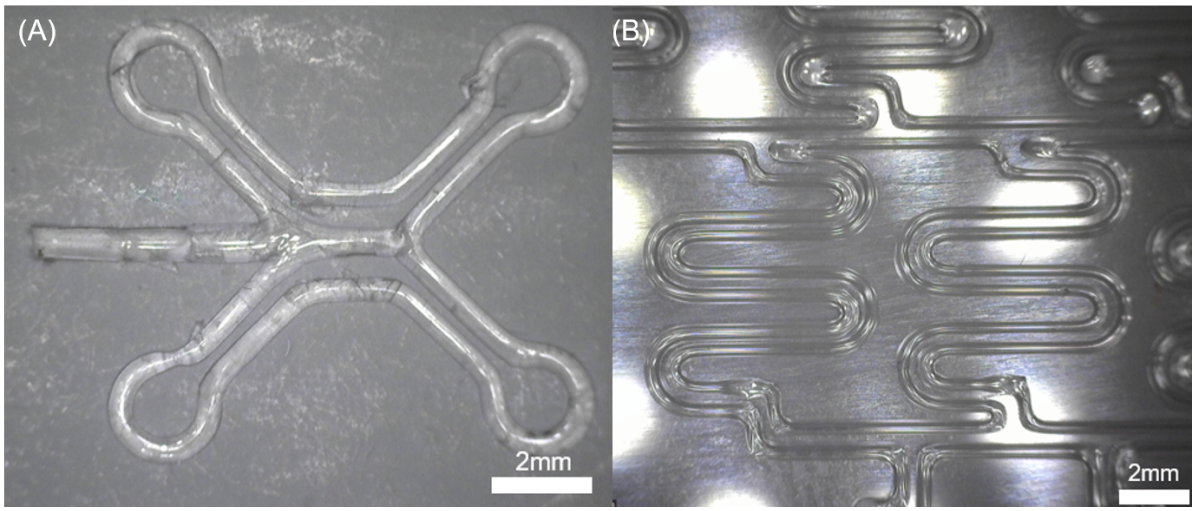

Figure 2.9: Optical images of 3d printed PDMS structures: (A) microfluidic channels (B) gradient generator

Table 2.4: Comparison of designed and measured dimensions of 3D-printed PDMS microfluidic structures (mean values, n=5)

Structure	Region	Designed (µm)	Measured (µm)	Absolute error (µm)	Max–Min (µm)
A	Central channel	700	543	157	54
	Peripheral channel	410	314	96	32
	Inlet/outlet port[a]	850	724	126	27
B	Channel	300	268	32	157

[a] For the circular inlet/outlet port the designed value is the *radius*.

Figure 2.9 shows optical microscope images of two representative 3D printed PDMS microfluidic structures. Image (A) presents a four-arm microfluidic channel with a central junction and circular inlet/outlet ports, while image (B) displays a gradient generator composed of multiple curved serpentine channels. Both designs were printed using a DIW method and assessed for dimensional fidelity.

Table 2.4 summarizes the comparison between designed and measured dimensions for different regions of the printed structures. For Structure A, the central channel was designed with a width of 700 µm, but the average measured width was 543 µm, resulting in an absolute error of 157 µm and a variation range (Max–Min) of 54 µm. The peripheral channels showed a designed width of 410 µm and a measured width of 314 µm, corresponding to a 96 µm absolute error and a 32 µm range. The inlet/outlet ports were designed with a radius of 850 µm, while the printed structures had an average radius of 724 µm, producing an absolute deviation of 126 µm and a variation of 27 µm.

For Structure B, the designed channel width was 300µm, and the actual printed width averaged 268µm, with an absolute error of 32µm. However, this region exhibited the highest variability among all structures, with a Max–Min spread of 157µm.

2.3. Discussion

2.3.1. Rheological Properties and Their Implications for Printing

The rheological analysis of PDMS blends revealed distinct differences in viscosity curves depending on the ratio of SE1700 to Sylgard 184, as shown in Figure 2.4 and Table 2.1. All formulations containing SE1700 (10:0, 9:1, 8:2, and 7:3) exhibited pronounced shear-thinning behavior, an ideal characteristic for DIW applications. Specifically, the viscosity of these inks dropped sharply from the low shear-rate region (0.1 s^{-1}) to around 10 s^{-1}, followed by a more gradual decrease up to 1000 s^{-1}. This behavior supports the presence of a structured internal network that breaks down under shear, allowing smooth extrusion through the nozzle, and then sufficiently recovers after deposition to maintain the fidelity of the printed shape.

The highest viscosity was observed in the pure SE1700 ink (10:0). As the Sylgard 184 content increased, the viscosity decreased significantly, suggesting that Sylgard acts as a diluent, reducing network density and flow resistance. At a shear rate of 100 s^{-1}, all SE1700-containing inks converged to a similar viscosity level (60–70 Pa·s), indicating that regardless of SE1700 content, the viscosity gradually plateaued as the shear rate increased. At 1000 s^{-1}, their viscosities further decreased to the range of 5–12 Pa·s. In contrast, the 0:10 formulation composed entirely of Sylgard 184 exhibited Newtonian behavior, maintaining an almost constant viscosity of 12 Pa·s across the entire shear-rate range. This result confirms the absence of shear-sensitive microstructures in Sylgard-only systems, whereas adjusting the SE1700-to-Sylgard ratio effectively tunes the shear-thinning properties of the inks.

The oscillatory amplitude sweep results of PDMS showed that the formulations containing SE1700 (10:0, 9:1, 8:2, 7:3) exhibited a G′ that significantly exceeded the G″ at low strain amplitudes, indicating that these inks displayed more gel-like characteristics. The yield point defines the threshold for permanent structural deformation and reflects the sample's stability (i.e., its resistance to internal sedimentation). As the proportion of Sylgard 184 in the ink increased, the yield point shifted to higher values. When the applied shear strain exceeded this threshold, the structure began to deform permanently, and the material started to flow like a liquid. Because the structural strength of the inks is reflected by the magnitude of G′, ink 10:0 exhibited the highest structural strength, while ink 0:10 showed the lowest. The 0:10 ink, composed solely of Sylgard 184, behaved as a liquid across all shear strains, as G″ dominated its response. Consequently, this type of ink exhibited no discernible yield point. Attempts to perform extrusion printing with ink 0:10 failed because the printed filaments could not retain their shape.

The frequency sweep test results for inks 9:1, 8:2, and 7:3 showed that G′ exceeded G″ at all frequencies, indicating that the inks would not spontaneously relax, collapse, or flow inside the syringe.

Overall, the rheological tests of the PDMS inks demonstrated that SE1700 is crucial for adjusting the printability of the inks. As the proportion of SE1700 increases, both the viscosity and structural strength of the ink increase. However, excessively high viscosity may lead to nozzle clogging. In contrast, pure Sylgard 184 ink lacks shear-thinning behavior and exhibits fluid-like characteristics under all shear stresses, making it non-printable.

2.3.2. Factors Affecting PDMS Printability

The dual-layer printing tests showed that printing quality and pore clarity were influenced by both the ink formulation and the syringe displacement. The 9:1 ink, with the highest SE1700 content, failed to form stable porous structures under low extrusion conditions (0.4 and 0.7 mm). This is likely due to its excessively high viscosity and the lack of support at the bottom, causing interruptions in filament deposition. In contrast, for the 8:2 ink, reducing the displacement from 1.0 mm to 0.4 mm led to a decrease in the extruded filament width, which directly resulted in an increase in pore area and a corresponding increase in perimeter. At the same time, its printability gradually approached 1. Additionally, for each displacement level, the upper layer structure showed slight sagging. The 7:3 ink exhibited similar behavior, but at low displacement (0.4 mm), the filament width was too small, causing the upper filaments to collapse severely onto the bottom layer. As a result, the ideal square pores transformed into hexagon-like shapes, leading to a reduction in the Pr. At high displacement (1.0 mm), the excessive extrusion caused the upper and lower layers to fully merge, with ink accumulating at the intersections to form rounded pores.

Overall, the dual-layer printing tests confirmed that printing double-layer structures with these inks

remains challenging. For high-structural-strength inks (9:1), the unsupported overhanging regions in the second layer could not sag due to the high G′, leading to interruptions in the suspended segments. For low-G′ inks, insufficient structural strength resulted in sagging and low printability. The 8:2 ink, with its intermediate G′, achieved higher printability, though some sagging still occurred (the widths of the overhanging segments were slightly smaller than those of the supported segments).

The results of the filament width tests indicate that the final filament width is determined by multiple interacting factors. First is the ink formulation. When printed with the same nozzle size, different ink ratios yielded different results. As the proportion of SE1700 increased, the printed filament width decreased. This is because inks with higher G′ more readily retain their original shape after extrusion without spreading, and under the same syringe displacement, inks with a higher SE1700 content extrude more slowly, resulting in narrower filaments. Second is the nozzle size. When the nozzle tip diameter decreased from 260 µm to 210 µm, the filament width showed a clear reduction. However, with a further decrease to 160 µm, the 9:1 ink produced discontinuous filaments, while the 8:2 and 7:3 inks were still able to form continuous filaments, but with increased widths. This occurs because at the same displacement level, a smaller nozzle tip significantly increases the shear strain on the ink, which markedly reduces both G′ and G″ during extrusion, with G″ exceeding G′, thereby increasing flowability. Third is the syringe displacement. A larger displacement produces wider filaments and allows for faster printing. This is because a higher displacement leads to a larger extrusion volume per unit time; at the same printing speed, the filament width therefore increases. Lastly is the printing speed. Generally, increasing the printing speed decreases filament width. However, excessively high speeds may lead to discontinuous filaments, while overly low speeds may cause ink accumulation at the nozzle tip. In summary, achieving the desired printing performance and minimizing filament width requires a balanced optimization of these four parameters.

The dimensional fidelity of 3D-printed PDMS microfluidic structures was evaluated by comparing the designed and measured dimensions of different geometric features in two representative designs. For both structures, the measured widths were smaller than the designed widths, with absolute errors ranging from 32 µm to 157 µm. This discrepancy can be attributed to several factors: the limited resolution of the DIW printer, the mismatch between the actual filament width and the filament width defined in the slicer software, and the gradual recovery of the ink's G′ and G″ after printing, which allows slight filament spreading during the transition from printing to final curing.

In the microfluidic channel structures, both circular and linear sections exhibited relatively small deviations (less than 60 µm). In contrast, the gradient generator channels showed the largest deviation (157 µm), with the narrowest region occurring at the U-shaped corner and the widest region at the right-angle entry of the U-shaped channel. In addition to the factors mentioned above, this can also be explained by the adhesion of the filament to the glass slide and the traction exerted by subsequently deposited filaments during printing. When printing sharp corners, this effect causes the actual sample to form a slight curve, widening the right-angle entrance. Conversely, when printing curved channels, the actual radius tends to be smaller than the design, leading to narrower U-shaped corners. To mitigate these effects, channel widths should be re-optimized at the design stage to compensate for dimensional deviations inherently introduced by the printing process.

2.3.3. Advantages and Limitations of DIW

DIW offers a mold-free route that greatly accelerates design–build–test cycles: layouts can be edited and printed within hours without the lead times of mask fabrication or wafer processing. Because the rheology of PDMS inks is tunable (by blending shear-thinning SE1700 with Sylgard 184), extrusion pressure, filament continuity, and shape retention can be optimized for specific geometries. The process uses equipment at low temperatures, which lowers cost and simplifies operation. In addition, printed PDMS preserves optical transparency and gas permeability, which supports imaging and long-term cell culture, making DIW attractive for early-stage neural platform prototyping.

However, there are some limitations that matter for axon-guidance microstructures. First, geometric resolution and fidelity are constrained by nozzle diameter, shear-thinning during extrusion, and post-deposition filament spreading; in the measurements, microchannel deviations ranged approximately from 32 to 157 µm depending on feature and layout. Second, multilayer features with overhangs are sensitive to mechanical support from the underlying layer; excessive spans promote sagging or merging of filaments, and the printability metric (Pr) departs from unity as pores distort. Third, the usable rheology window is narrow: inks that are too viscous risk discontinuities and clogging, while inks that are too

fluid lose definition. The coupled nature of speed, displacement, nozzle size, and ink composition also means that parameter changes can have non-intuitive effects (e.g., smaller nozzles producing wider lines due to elevated shear and slow recovery). Finally, although PDMS is biocompatible, the long-term stability and guidance efficacy of DIW-printed microchannels still require systematic validation.

3

Microfabrication of PDMS Microfluidics

3.1. Materials and Methods

3.1.1. Mask Design

The photomask used for microfluidic device fabrication was designed using K-Layout (version 0.30.0), a layout editor compatible with GDS format. The mask adopts a single-layer design intended for PDMS casting based on soft lithography. As shown in Figure 3.1, the complete mask layout consists of 21 identical microfluidic structures uniformly arranged on a single foil mask to facilitate batch manufacturing.

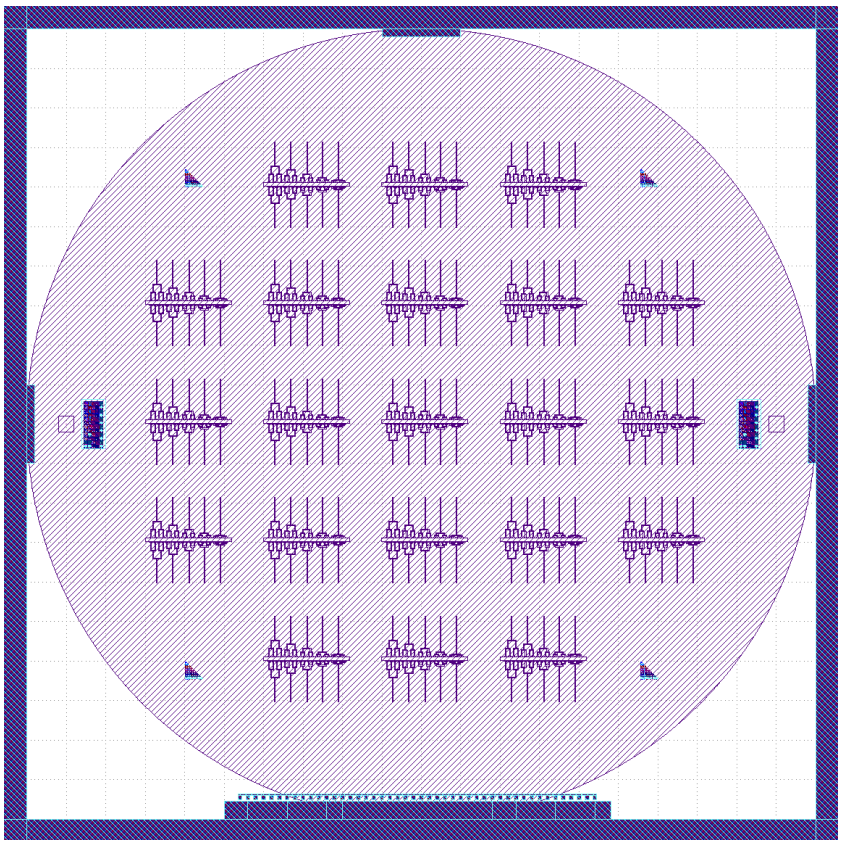

Figure 3.1: The foil mask layout

Each individual microfluidic structure, as illustrated in Figures 3.2 and 3.3, exhibits symmetry and comprises two major functional regions: a central main channel, 500µm in width, which is designed for cell seeding; and branch regions on both sides, each extending 5000µm in total length and 100µm in width, which contain multiple subchannels that guide axonal growth. Each branch is further subdivided into three distinct functional zones: Nerve bundle channels: Straight channels region that allow axons to interconnect and form nerve bundle. Axon guidance channels: Designed to generate axon guidance channels of different lengths to evaluate the impact of guidance length on nerve bundle formation. From left to right, the lengths of guidance channels are: 2000µm, 1500µm, 1000µm, 500µm, and 250µm. Cell body blocking channels: Located at the distal end of each guidance channel, these restrictive channels are intended to block cell bodies from the outside but allow axons to grow inside. Two sets of photomask designs were created, each incorporating cell body blocking channels with different widths (5 µm and 10µm), enabling comparative analysis of axon penetration under varying physical constraints. Each cell body blocking channel is connected to its respective guidance channel via a funnel-shaped transition region. The layout was exported in GDSII format and submitted for high-resolution chrome mask fabrication, enabling precise pattern transfer during the photolithography process.

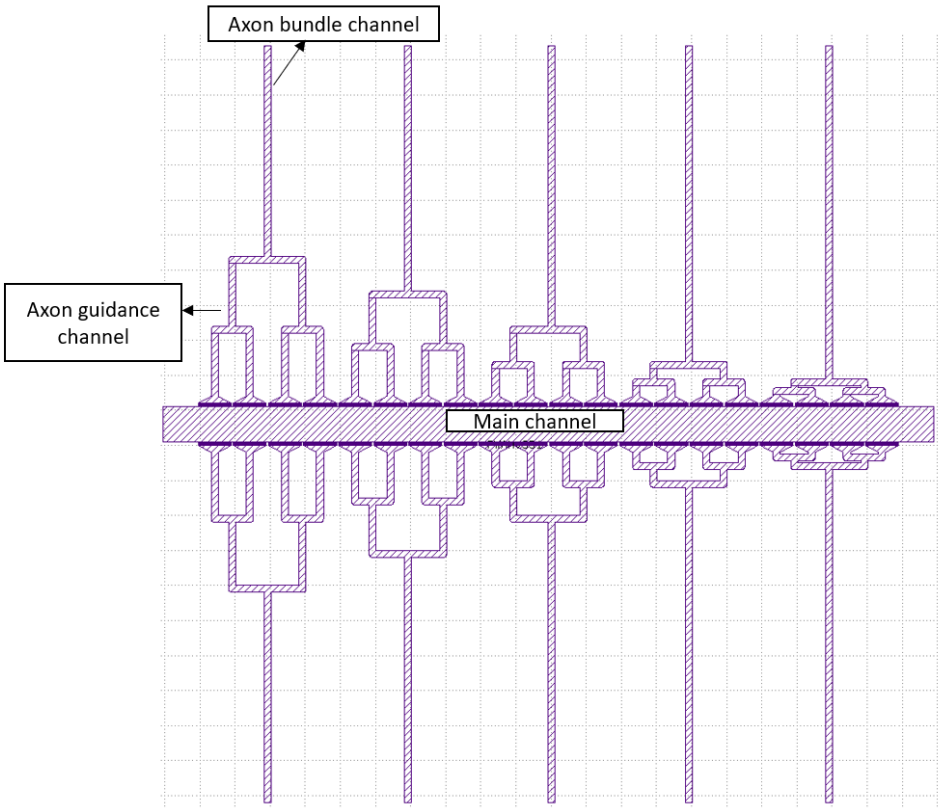

Figure 3.2: Schematic layout of the microfluidic structure for axon guidance

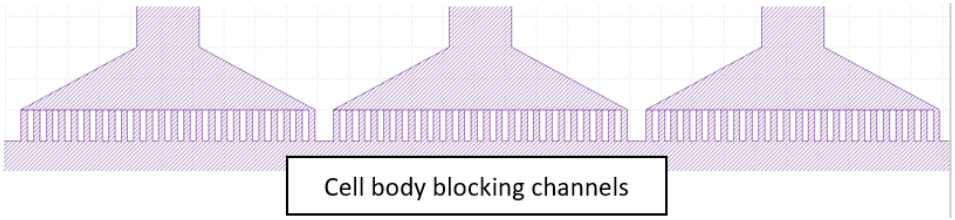

Figure 3.3: The cell body blocking channels

3.1.2. Fabrication of the Microfluidic Structures

The fabrication of the microfluidic structures consisted of the following seven steps. The first five steps were used to produce the silicon master mold, while the final two steps were used for PDMS–PDMS double casting.

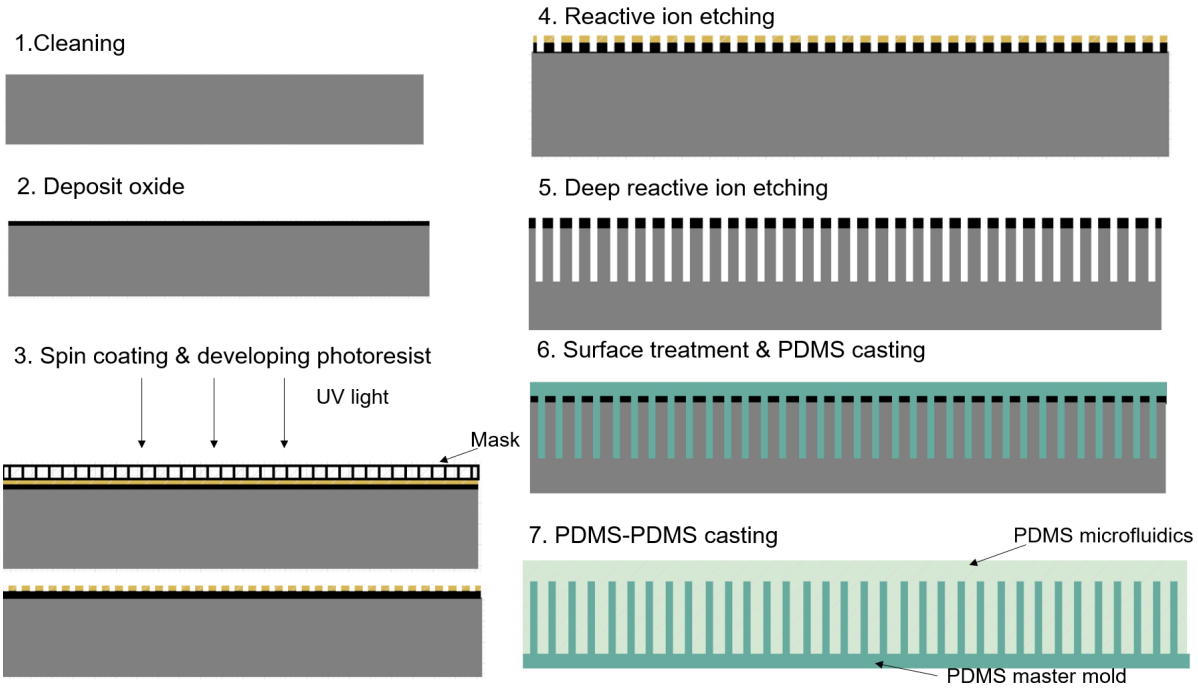

Figure 3.4: The flowchart of microfluidic structures fabrication

1.Wafer cleaning The silicon wafer is first immersed in 99 % HNO_3 in a wet bench for 10 minutes to strip away organic residues. After a 5-minute rinse in deionized water, the wafer is transferred to a 69.5 % HNO_3 bath for another 10 minutes to remove any metal particulates, followed by a second 5-minute rinse in deionized water. Finally, the wafer is dried under a nitrogen stream to ensure a clean, particle-free surface.

2. Oxide deposition A uniform, 3000 nm-thick layer of silicon dioxide is deposited onto the cleaned wafer using plasma-enhanced chemical vapor deposition (PECVD) in a Novellus Concept 1 tool. This oxide layer will act as the hard etch mask for all subsequent pattern transferring steps.

3. Photoresist spin-coating and development AZ ECI 3027 positive photoresist is spin-coated to a thickness of approximately 2.3 µm using the EVG 120 coater-developer. The coated wafer is on a SUSS MicroTec MA/BA 8 mask aligner and exposed to ultraviolet light, transferring the pattern into the resist. Development removes the exposed resist, leaving behind a precise photoresist template at the top of the oxide.

4. Reactive ion etching In a Drytek Triode 384T etcher, a fluorine-based plasma is used to anisotropically etch the exposed silicon dioxide, transferring the photoresist pattern into the underlying oxide and forming a durable hard mask.

5. Deep reactive ion etching Using a Rapier Omega i2L DRIE system and the Bosch “etch/passivation” cycle, the etch rate of the system was 0.72 µm per loop. To achieve 100µm-deep, HAR pillars, 139 loops were performed to etch the features into the silicon substrate. After completing the silicon etch, a thin teflon passivation layer was deposited at the bottom of the structures to reduce adhesion between the silicon master and the subsequent PDMS replicas.

6. PDMS casting and surface treatment The PDMS prepolymer is prepared by mixing the base and curing agent in a 10:1 weight ratio, then poured over the etched silicon master. The wafer carrying liquid PDMS is placed in a vacuum degasser for 15 minutes to remove air bubbles, then transferred to an oven and cured at 100 °C for one hour. Once cured, the PDMS master mold is carefully peeled from the silicon wafer with tweezers. Because PDMS adheres strongly to itself, the demolded master mold must undergo anti-adhesion treatment before it can serve as a mold for a second PDMS

cast. A vapor-phase silanization is performed by introducing a few drops of trichloro(1H,1H,2H,2H-perfluorooctyl)silane (PFOCTS) into a sealed container with the PDMS master, pumping down to vacuum, and leaving overnight. This treatment deposit a thin anti-adhesive layer that facilitates easy separation of subsequent PDMS replicas.

7. PDMS-PDMS double casting PDMS (10:1 base to curing agent by weight) is poured over the surface-treated PDMS master mold and degassed under vacuum for 15 minutes to eliminate any air bubbles. The mold is then cured in an oven at 100 °C for one hour. During demolding, the newly cured PDMS replica is slowly peeled away along the length of the microchannels to minimize shear forces. A small amount of ethanol is introduced at the PDMS–PDMS interface to further reduce friction.

Additionally, an alternative method was employed in this study to fabricate microfluidic structures by etching the regions outside the desired patterns, allowing PDMS to be directly cast onto the wafer to form the microfluidic channels. The fabrication of the wafer mold generally followed the same five steps described above. However, a key difference was the use of a negative photoresist (AZ nLOF 2020), which was spin-coated to a thickness of 2 µm onto a wafer pre-coated with a SiO_2 layer. After UV exposure, the unexposed photoresist was removed using a developer, leaving the exposed, patterned areas covered with resist. Using the same RIE and DRIE settings, the patterned regions remained higher relative to the etched surroundings on the wafer, enabling direct PDMS casting to obtain the final microfluidic structures.

3.1.3. Characterization

Three distinct silicon molds were evaluated: a 10 µm positive mold, a 5 µm positive mold, and a 10 µm negative mold. Here, “positive” indicates that the features were etched into the wafer, whereas “negative” means that material outside the pattern was removed. “5 µm” or “10 µm” refers to the width of the cell body blocking channels. All measurements were performed on a Keyence VK-X250 confocal laser scanning microscope. On each wafer, two regions were measured to quantify etch depth and surface roughness: the main channel and axon guidance channels. In addition, the aspect ratio of the cell body blocking structures was calculated from the measured channel depths and widths.

Replication fidelity and demolding performance were first assessed by optical inspection of the PDMS master molds cast from the 5 µm and 10 µm wafers using the Keyence VK-X250. These observations confirmed whether fine features from the wafer mold were faithfully reproduced and whether the PDMS masters could be cleanly separated from their molds. Because the confocal profiler has limited accuracy on transparent samples, PDMS molds and their corresponding final microfluidic devices that passed the optical observation were further characterized by scanning electron microscopy (Hitachi Regulus 8230). SEM images of the main channels, axon guidance channels, and cell-body-blocking channels were used to precisely measure feature depth, surface roughness, and aspect ratio in the transparent PDMS structures.

3.2. Results

3.2.1. Wafer Mold Characterization

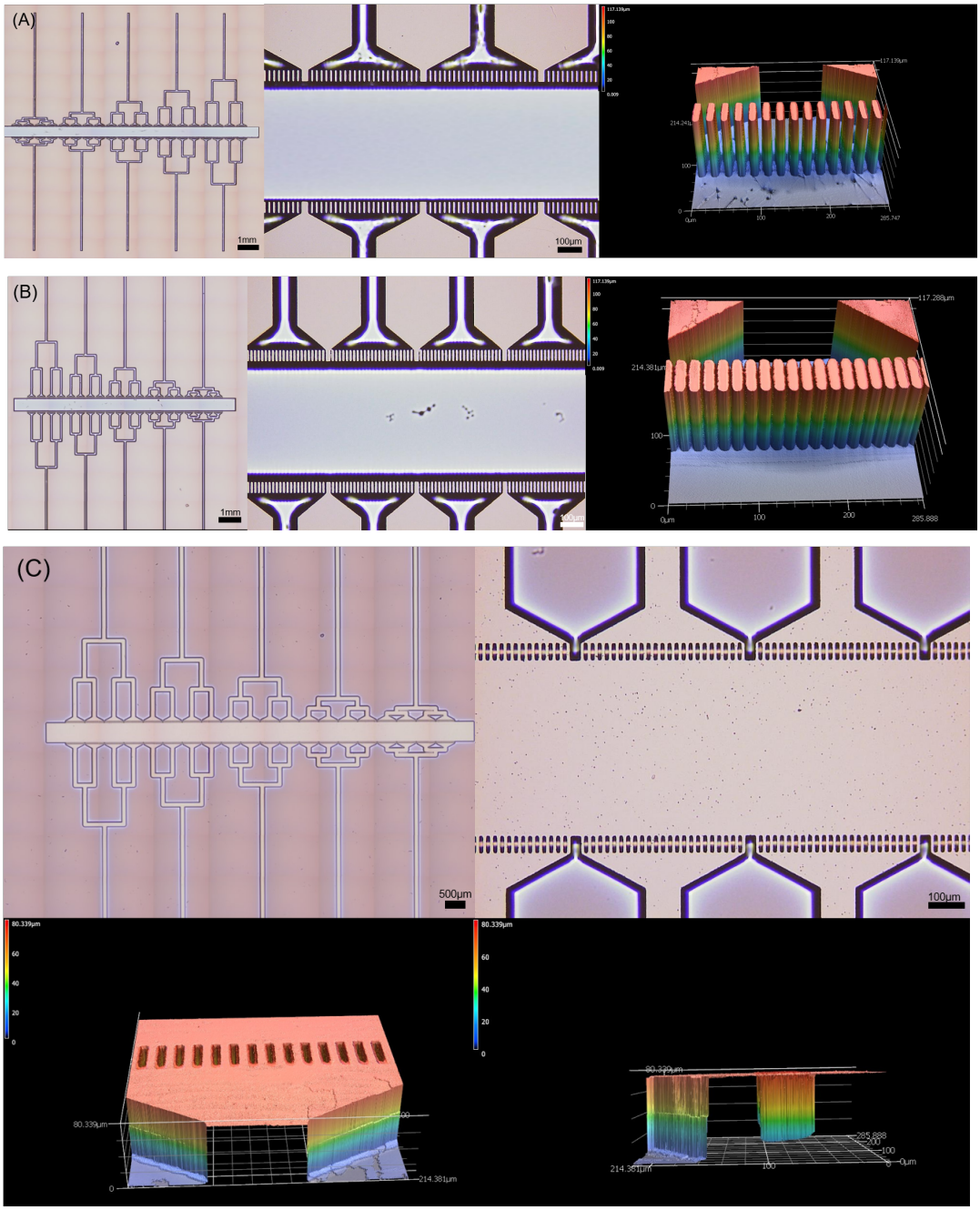

Figure 3.5: Optical images of wafer molds: (A)10 µm positive mold, (B)5 µm positive mold, and (C)10 µm negative mold (top to bottom).

Table 3.1: Summary of morphological parameters of wafer molds

Wafer mold	Region	Average height/depth (µm)	Average roughness R_a (µm)
10 µm Positive Mold	Main channel	106.578	0.730
10 µm Positive Mold	Axon guidance channels	103.588	1.026
5 µm Positive Mold	Main channel	107.533	0.777
5 µm Positive Mold	Axon guidance channels	103.907	1.265
10 µm Negative Mold	Main channel	72.286	0.145
10 µm Negative Mold	Axon guidance channels	73.364	0.184
Aspect ratio of cell blocking channels			
10 µm Positive Mold	Cell blocking channels	8.712	
5 µm Positive Mold	Cell blocking channels	8.773	
10 µm Negative Mold	Cell blocking channels	6.108	

Table 3.1 summarizes the morphological characteristics of three wafer mold types, including their average feature height, surface roughness, and aspect ratio. For all designs, the target height was 100µm and the ideal aspect ratio was 10.

For the 10 µm positive mold, the main channel exhibited an average height of 106.578 µm with a surface roughness of 0.730 µm. The axon guidance channels in the same mold had a slightly lower average height of 103.588 µm and a higher roughness of 1.026 µm. The 5 µm positive mold showed similar trends, with the main channel height averaging 107.533 µm (Ra = 0.777 µm) and the axon guidance channels measuring 103.907 µm in height with 1.265 µm surface roughness. In contrast, the 10 µm negative mold has significantly lower height values, with the main channel and axon guidance regions 72.286 µm and 73.364 µm, respectively. These structures also exhibited the smoothest surfaces, with Ra values of 0.145 µm and 0.184 µm, respectively. The aspect ratios of the cell blocking channels were also analyzed. The 10 µm and 5 µm positive molds have aspect ratios of 8.712 and 8.773, respectively, both close to the design goal of 10. However, the 10 µm negative mold presented a lower aspect ratio of 6.108.

3.2.2. PDMS Master Molds

PDMS master molds with micropillars of two different spacings (5 µm and 10 µm) were observed under a confocal microscope and SEM, as shown in Figures 3.6 and 3.7.

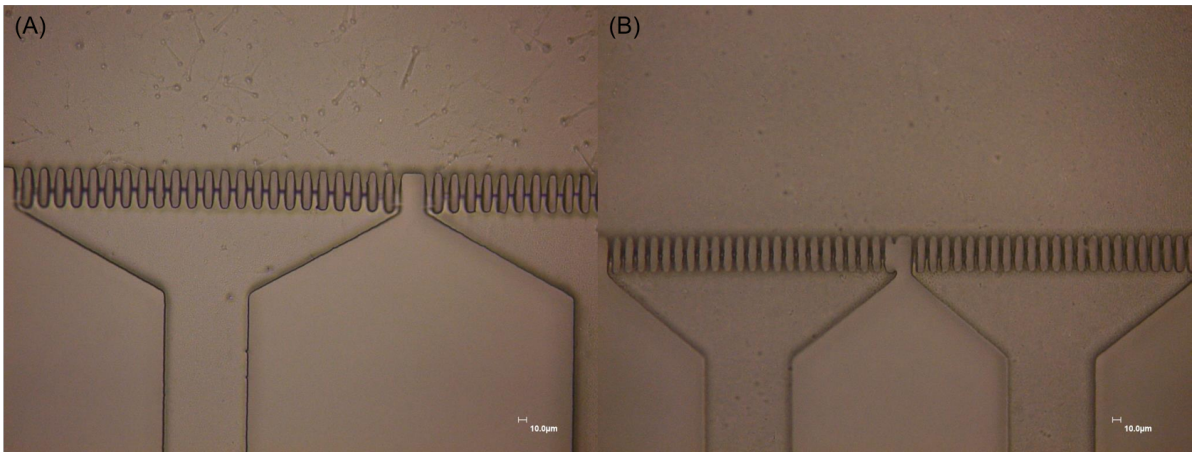

Figure 3.6: Optical images of PDMS master molds: (A) 10µm mold, (B) 5µm mold

Figure 3.6 shows optical microscope images of the PDMS master molds fabricated with different feature sizes. Figure (A) corresponds to the 10 µm mold, while Figure (B) shows the 5 µm mold. The 10 µm mold displays well-defined microchannel structures and clear boundaries between the axon guidance channels and the wider main channels, whereas in the 5 µm mold, adhesion occurred in some of the channels.

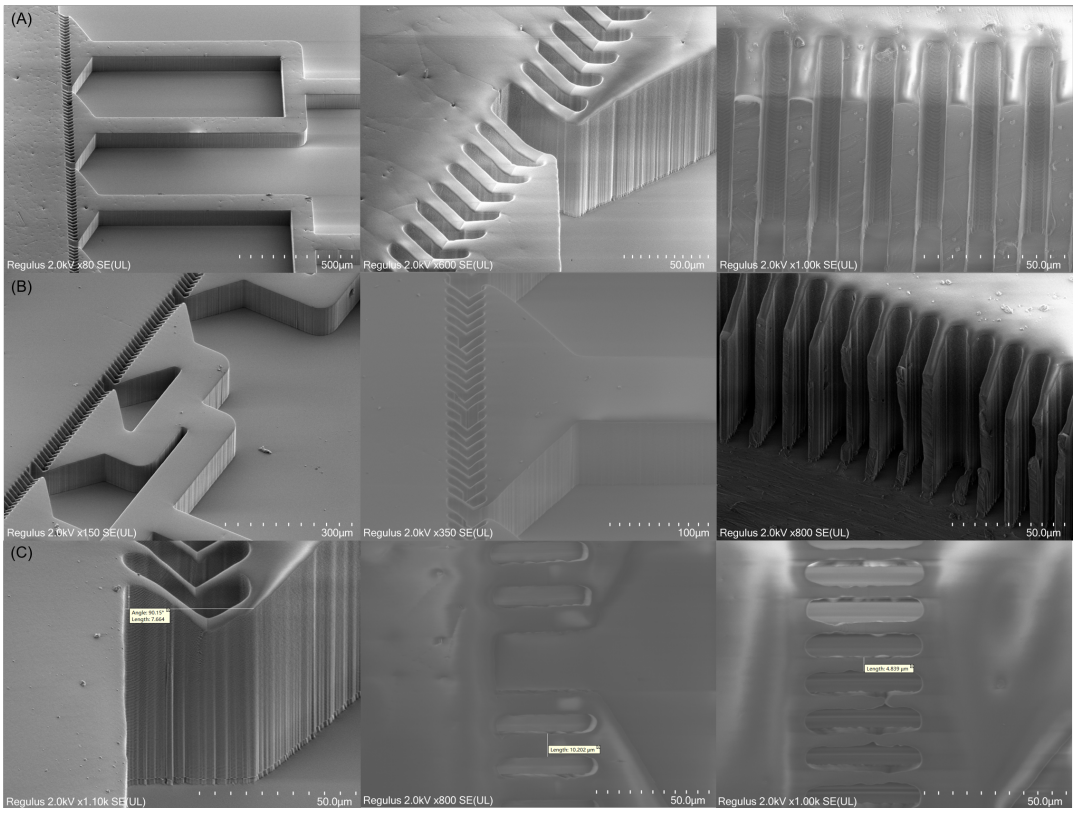

Figure 3.7: SEM images of PDMS master molds: (A) 10µm mold, (B) 5µm mold, (C) measurements

Figure 3.7 shows the SEM images of the PDMS master molds. Figure (A) presents the 10 µm master mold at different magnifications. The left image demonstrates well-defined rectangular channels with uniform widths over a large area. The middle image shows periodically arranged, HAR pillar structures with steep vertical sidewalls, while the right image displays a cross-section of the cell body blocking channels, with no adhesion observed between adjacent structures. The surface smoothness and line spacing appear consistent across the entire field of view.

Figure (B) presents the 5 µm master mold. Due to the smaller feature size, slight tearing of the cell body blocking channels was observed, while the remaining features were replicated well. The SEM image on the right further confirms the presence of high density and HAR structures.

In addition, “V”-shaped profiles can be observed in both the 10 µm and 5 µm molds, indicating that the height of the main channels is actually greater than that of the axon guidance channels. Measurements show a marked height difference of 7.664 µm. Considering the 45° viewing angle, the actual height difference is estimated to be approximately 10.806 µm. The middle and right images also provide measured channel widths of 10.202 µm and 4.839 µm, respectively.

3.2.3. PDMS Master Mold and Microfluidic Structures after Demolding

Figure 3.8 shows optical microscope images of the PDMS master molds and the corresponding microfluidic structures after the demolding process. Figure (A) presents the original master molds, with the upper and lower panels corresponding to the 10 µm and 5 µm designs, respectively. The microstructures appear clean and intact; however, compared to the undemolded PDMS master molds, some tilting and misalignment are observed. Figure (B) shows the PDMS microfluidic structures obtained after demolding. Notably, the 5 µm structures exhibit severe structural damage, particularly in the cell body blocking channel regions, where vertical pillars collapse, shift, or even tear completely. In contrast, the 10 µm structures appear to retain most of their integrity under optical observation.

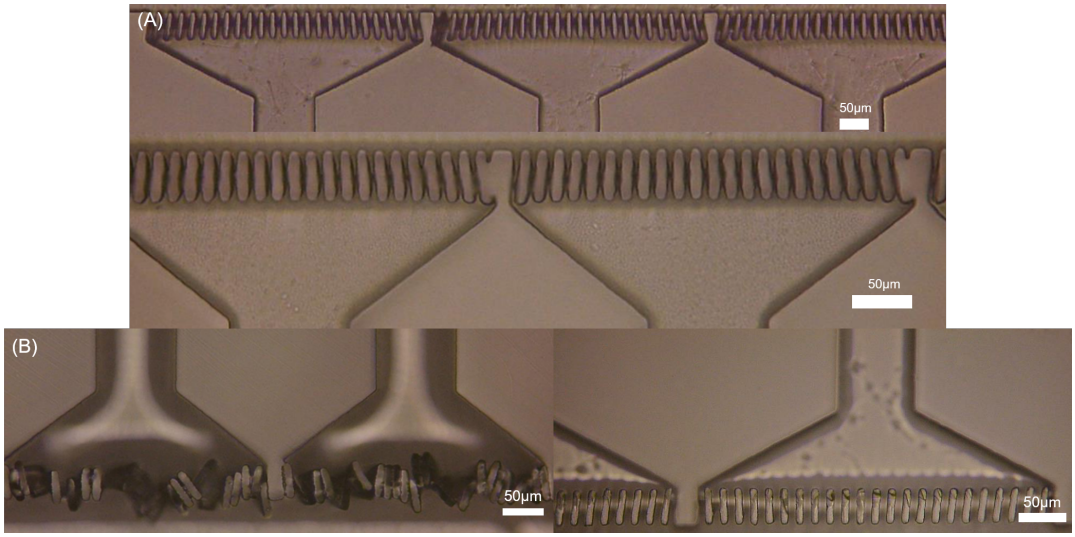

Figure 3.8: Optical images of PDMS master molds and microfluidic structures after demolding: (A) master molds (B) microfluidic structures

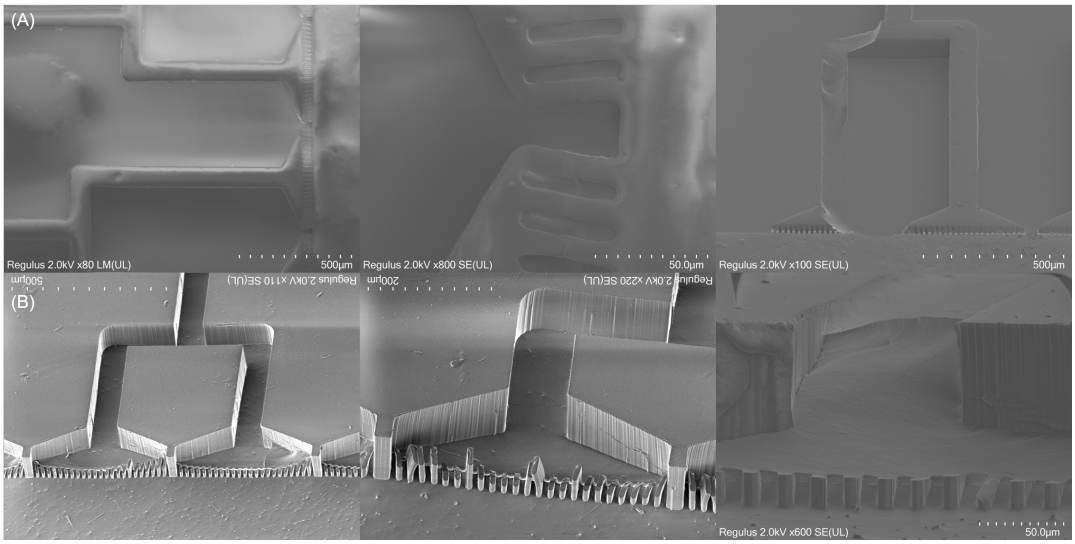

Figure 3.9: SEM images of PDMS 10µm master mold and microfluidic structures after demolding: (A) master mold (B) microfluidic structures

To further verify whether the 10 µm structures remained intact, the master mold and the corresponding microfluidic structures were further examined under SEM. Figure 3.9 shows the optical microscope images of the PDMS master mold and the corresponding microfluidic structures after the demolding process. Figure (A) presents the original master mold with well-defined microfeatures. Noticeable tilting was observed in the “cell body blocking channels,” and some axon guidance channels exhibited severe structural loss. Figure (B) shows the PDMS microfluidic structures produced after demolding, which display significant structural damage, particularly in the cell body blocking channel regions, where vertical pillars collapsed, became misaligned, or were even completely torn. In the axon guidance channels, residual PDMS from the master mold was also observed, indicating material transfer during demolding.

3.2.4. PDMS Microfluidic Structures Derived from Negative Wafer Mold

Figure 3.10 shows SEM images of PDMS microstructures obtained by direct casting from the negative wafer mold. The left image presents a low-magnification cross-sectional view of the entire microchannel region, while the right image provides a close-up of a high density and HAR feature.

The results confirm that the PDMS structures largely retained their overall structural integrity after demolding. The vertical micropillars and surrounding channel structures are well-defined, with no large-scale fractures or delamination observed. The bottom surface appears flat and clean, indicating good mold contact and uniform curing during the casting process. However, some defects are apparent. Certain PDMS pillars exhibit tilting, and slight adhesion between adjacent features can be observed, particularly near the top of the structures. In addition, the calculated aspect ratio of the micropillars is 5.932, which is close to the value previously measured for the wafer mold under a confocal microscope (6.108).

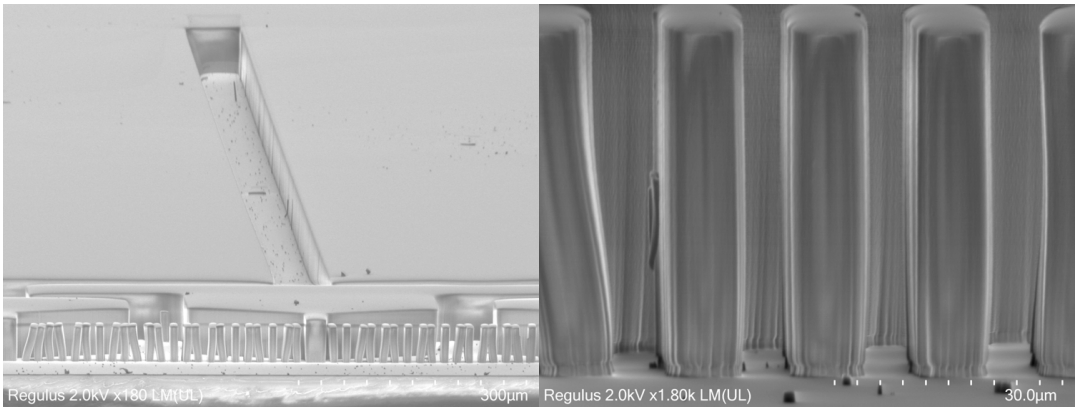

Figure 3.10: SEM Images of PDMS structures directly cast from negative wafer mold

3.3. Discussion

3.3.1. Wafer Mold Quality and Etching Depth

The morphological evaluation of microfabricated wafer molds provides valuable insights into the accuracy and quality of photolithographic pattern transfer, particularly in terms of height, surface smoothness, and feature fidelity.

Both positive molds exhibited average feature heights slightly higher than expected, indicating that the number of DRIE etching cycles was slightly above the intended value. For both positive wafer molds, the average etching depth of the main channels was higher than that of the axon guidance channels, while their average roughness was lower. This is because the main channels are 500 µm wide, compared to 200 µm for the axon guidance channels. During the etching process, SF6 gas penetrates narrow channels less efficiently, resulting in a higher effective etching rate in the wider main channels. Moreover, due to the etching rate differences: main channel > axon guidance channels > cell body blocking channels, a “V”-shaped slope can be observed at the bottom of the cell body blocking channels. This feature is more clearly visible in SEM images of the PDMS master molds.

In contrast, the average height of the 10 µm negative mold was significantly lower. This is because the DRIE etching rate is calibrated for standard positive molds, which only require etching of patterned areas. Negative molds, however, require etching of all regions except for the pattern, covering over 90% of the wafer surface, which results in a lower effective etching rate. Additionally, because the cell body blocking channels are only 10 µm wide, gas penetration is even more limited. This is shown in the 3D surface profiles, where the depth of these narrow regions is shallower than that of the surrounding features, contributing to a lower aspect ratio.

Surface roughness is another critical indicator of mold quality and varied across the three molds. The negative mold exhibited the smoothest surface because its roughness reflects the deposited SiO2 layer, which is not etched during the DRIE process. By contrast, the roughness of the positive molds was slightly higher due to direct silicon etching. Among the positive molds, the main channels showed higher roughness than the axon guidance channels, indicating that etching in the main channels was more uniform.

3.3.2. PDMS–PDMS Double Casting and Failure Analyses

The PDMS master mold peeled from the wafer exhibited good fidelity in replicating fine details. Measurements showed that the widths of the cell body blocking channels closely matched the theoretical values. Additionally, a height difference between the main channel and axon guidance channels was observed, along with the “V”-shaped profile. However, damage was found in the 5 µm-wide blocking channels. This damage resulted from friction between the wafer sidewalls and the cured PDMS during demolding. Compared to the 10 µm structures, the 5 µm channels are thinner and more prone to tearing.

When PDMS was cast onto the PDMS master mold and subsequently peeled off, the blocking channels on the master mold exhibited noticeable misalignment. Despite surface passivation of the mold and a relatively smooth demolding process, friction between the replica and the mold led to two issues: first, parts of the mold’s channels were torn off and adhered to the replica; second, the blocking channels on the replica were severely deformed. The failures of the replicas can be categorized into two main types: lateral collapse and longitudinal tearing.

When high aspect ratio structures are densely packed, lateral collapse can spontaneously occur if the elastic restoring force generated by elastic strain is insufficient to overcome the surface adhesion between adjacent structures. Researchers have investigated the potential for lateral collapse of elastomeric structures during demolding, which is described by the following equation [53]:

$$\frac{h}{2a} < \left(\frac{2Ew^2}{\gamma_s a}\right) \tag{3.1}$$

where h is the structure height, $2a$ the line width, $2w$ the spacing between adjacent structures, E the Young’s modulus, and γ_s the surface tension.

The formula indicates that collapse is more likely to occur when the structures are taller, narrower, more closely spaced (as shown in Figure 3.11), or made from softer materials with lower elastic moduli. For PDMS micropillars, structures that are 10 µm wide, with an aspect ratio of 8 and a spacing of 10 µm, are prone to such failure.

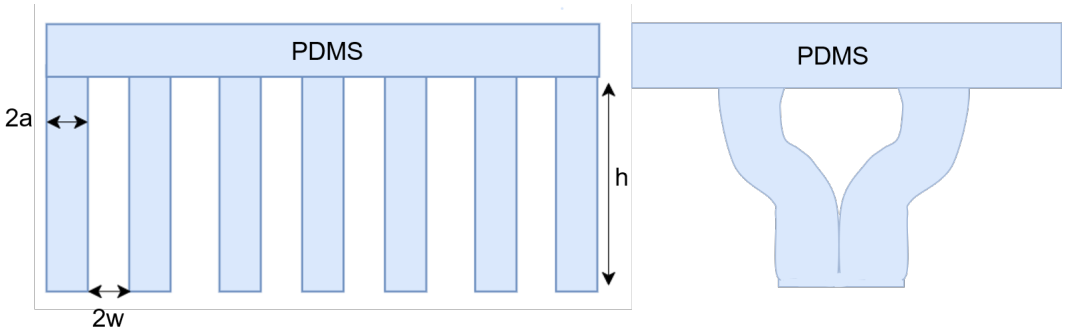

Figure 3.11: Illustration of lateral collapse

Longitudinal tearing refers to the phenomenon during demolding in which the replica is subjected to friction against the mold, causing the raised features on the replica to be significantly stretched (as shown in Figure 3.12). The stress induced by this friction can exceed the maximum mechanical strength of the structure, leading to fracture at the top. Another possible reason is that, since PDMS is not a rigid material when used as a master mold, it may bend during the demolding process. The bending of the micropillars can cause stress concentration at the bending points, which may eventually lead to fracture.

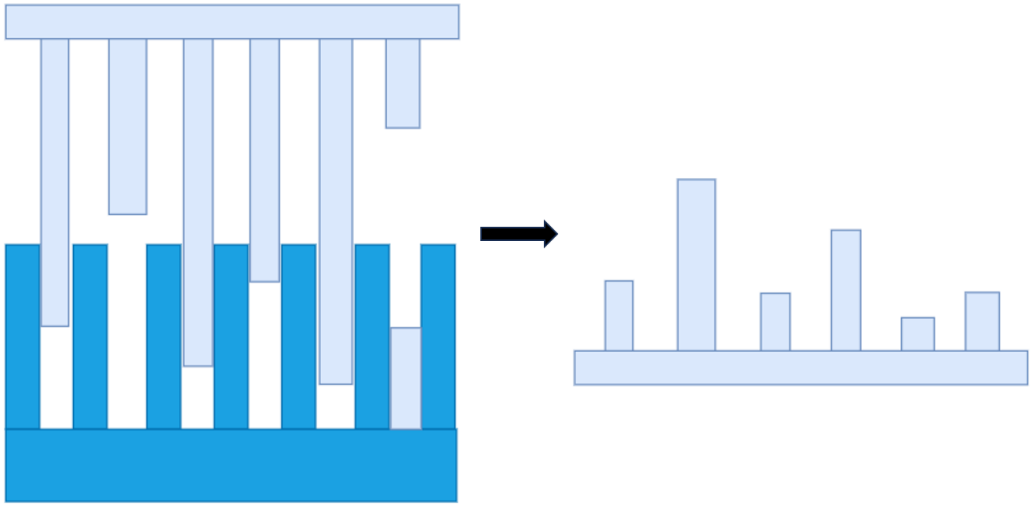

Figure 3.12: Illustration of longitudinal tearing

3.3.3. Direct Demolding from Negative Wafer Mold

The PDMS microfluidic structures directly demolded from the negative wafer mold exhibited high structural fidelity. Although slight lateral collapse was observed, this is attributed to the elastic rebound of micropillars during extraction from the mold, as no spontaneous lateral collapse occurred post-demolding. Additionally, no longitudinal tearing was observed, and the channel bottoms remained flat without forming V-shaped slopes. These observations indicate that the spacing and aspect ratio of the high-density axon-blocking channels were close to the theoretical threshold for lateral collapse. The absence of longitudinal tearing can be explained by two factors. First, the micropillars are relatively short, resulting in a limited elastic strain length under frictional forces during demolding, thereby reducing the likelihood of tearing. Second, the wafer mold can be regarded as a rigid body, which does not deform during the demolding process, thus minimizing bending or breakage of the micropillars.

3.3.4. Advantages and Limitations of Microfabrication

Cleanroom microfabrication combines photolithography with deep reactive ion etching to deliver micron-precision, HAR features with steep sidewalls—well suited to axon–soma compartmentalization and directional guidance. Wafer-scale patterning generate many identical devices per run, improving uniformity and reproducibility for biological comparisons. PDMS replicas cast from silicon molds remain optically clear and are readily aligned to MEAs, facilitating integration for stimulation and recording. In the study, direct PDMS casting from negative silicon molds preserved dense arrays and improved geometric fidelity relative to PDMS–PDMS double casting from positive masters, while durable silicon tooling supported repeated use.

The method's drawbacks are largely practical. Process complexity and cost are higher than DIW, requiring masks, multiple deposition/etch steps, and access to cleanroom infrastructure. Demolding remains a critical failure point for dense HAR patterns: during PDMS–PDMS double casting, we observed lateral collapse and longitudinal tearing of slender features, whereas negative silicon molds mitigated these issues but did not eliminate. Aspect- and width-dependent etch rates in DRIE introduce depth non-uniformity (e.g., shallower narrow channels and V-shaped bottoms), which may necessitate staged patterning/etching or design compensation. Planarity constraints limit truly three-dimensional topologies without additional stacking and bonding, and overall turnaround, dominated by mask lead time and queueing, slows iteration compared with DIW.

4

Conclusion

4.1. Conclusion

This thesis presents a comprehensive investigation into the development of PDMS-based microfluidic platforms for in vitro axon guidance, utilizing both DIW and cleanroom microfabrication techniques. The objective was to fabricate microstructures capable of mimicking the structural and functional compartmentalization of neuronal tissues, thereby enabling high-resolution studies of axon guidance.

In the first part of the study, a series of PDMS inks were formulated by blending shear-thinning SE1700 with low-viscosity Sylgard 184 at varying ratios. Rheological characterization revealed that increasing the SE1700 content significantly enhanced both the viscosity and elastic modulus of the inks, improving shape retention during printing. The 8:2 formulation exhibited the best balance between printability and structural fidelity, as confirmed by dual-layer pore formation and filament width analysis. In contrast, the 9:1 ink was too viscous to extrude under low-pressure conditions, whereas the 0:10 ink lacked sufficient yield stress to maintain printed shapes. These findings underscore the critical role of tuning viscoelastic properties to meet DIW printing requirements.

Beyond rheological optimization, a detailed investigation into filament width in relation to nozzle size, printing speed, and syringe displacement highlighted the complex interconnection between processing parameters and final structural resolution. Notably, unexpected filament widening was observed when using the smallest nozzle (160 µm), likely due to the ink transitioning into a fluid-like state under high shear and recovering its gel-like behavior more slowly. These insights offer guidance for achieving high-resolution patterning with PDMS.

The second part of the study focused on the fabrication and characterization of silicon molds using photolithographic techniques. Positive molds fabricated via DRIE produced HAR features (>8:1) with sub-10 µm resolution. However, PDMS–PDMS double casting using these molds presented mechanical challenges during demolding, including lateral collapse and longitudinal tearing of narrow structures. These failures were attributed to strong surface adhesion between adjacent micropillars and stress concentration at bending points during demolding.

To overcome these limitations, an alternative approach was adopted using etched negative silicon molds, onto which PDMS was directly cast. The resulting microfluidic structures exhibited improved geometric fidelity and mechanical robustness. Vertical micropillars retained their shape, and no longitudinal tearing was observed. Moreover, spontaneous lateral collapse did not occur, indicating that the combination of pillar spacing and aspect ratio (HAR = 5.932, spacing = 10 µm) remained within the threshold. Additionally, the inherent rigidity of the silicon wafer prevented substrate deformation during demolding, further reducing structural failure.

In conclusion, this work demonstrates that DIW enables rapid prototyping, while microfabrication offers high precision and reproducibility at the micron scale. The insights gained from this study, ranging from ink formulation and printability to mold performance and demolding mechanics, form a solid foundation for building reliable in vitro systems for axon guidance and neural interface research.

4.2. Recommendations

Further research is required to deepen the understanding and enhance the fabrication of PDMS-based in vitro platforms. Accordingly, the following recommendations are proposed:

1. **Multilayer printing with DIW:** When performing dual-layer printing using DIW, different ink formulations exhibit varying degrees of collapse. To achieve reliable dual- or multi-layer printing, the bottom layer must provide sufficient mechanical support for the overhanging segments of the upper layer. This implies that the span length and area of the overhangs critically influence printability, and should be carefully addressed during the design phase.
2. **Ink optimization:** Although the PDMS ink formulations tested in this work demonstrated satisfactory printability, further improvements are necessary to achieve higher printing resolution and long-term structural stability. Future efforts may explore the incorporation of nanoparticle additives (e.g., silica, graphene oxide) or rheology modifiers to enhance shear-thinning behavior without significantly increasing the risk of nozzle clogging. Additionally, active curing strategies such as in situ thermal crosslinking or UV-assisted crosslinking during extrusion may reduce filament spreading and improve feature fidelity.
3. **Depth control in wafer etching:** The fabrication process using photolithography and DRIE revealed inconsistencies in etching depth for structures of varying widths, particularly in narrow (10 μm) channels. A potential solution is to develop a staged patterning process, in which narrower channels are first developed and etched for several cycles, followed by patterning of wider features. This staggered etching approach would better compensate for the varying etch rates and help ensure consistent channel depths across different feature sizes.
4. **Toward functional neural platforms:** To translate these platforms into functional in vitro neural models, future work should incorporate long-term neuronal culture and axonal guidance studies. The integration of MEAs with PDMS-based axon guidance structures could enable real-time monitoring of neural activity, network formation, and synaptic connectivity. The platform developed in this study provides a foundation for demonstrating the feasibility of DIW-printed PDMS culture systems and the effectiveness of HAR, high-density axon guidance features in constructing engineered neural networks.

References

[1] Jaimie D Steinmetz et al. “Global, regional, and national burden of disorders affecting the nervous system, 1990–2021: a systematic analysis for the Global Burden of Disease Study 2021”. In: *The Lancet Neurology* 23.4 (2024), pp. 344–381.

[2] Sam Norton et al. “Potential for primary prevention of Alzheimer’s disease: an analysis of population-based data”. In: *The Lancet Neurology* 13.8 (2014), pp. 788–794.

[3] Günther Deuschl et al. “The burden of neurological diseases in Europe: an analysis for the Global Burden of Disease Study 2017”. In: *The Lancet Public Health* 5.10 (2020), e551–e567.

[4] Bart De Strooper and Eric Karran. “The cellular phase of Alzheimer’s disease”. In: *Cell* 164.4 (2016), pp. 603–615.

[5] Daniel H Geschwind and Genevieve Konopka. “Neuroscience in the era of functional genomics and systems biology”. In: *Nature* 461.7266 (2009), pp. 908–915.

[6] Liqun Luo. “Architectures of neuronal circuits”. In: *Science* 373.6559 (2021), eabg7285.

[7] Jin H Son et al. “Neuronal autophagy and neurodegenerative diseases”. In: *Experimental & molecular medicine* 44.2 (2012), pp. 89–98.

[8] Roberta Azzarelli et al. “In vitro, ex vivo and in vivo techniques to study neuronal migration in the developing cerebral cortex”. In: *Brain sciences* 7.5 (2017), p. 48.

[9] Cara L Croft and Wendy Noble. “Preparation of organotypic brain slice cultures for the study of Alzheimer’s disease”. In: *F1000Research* 7 (2018), p. 592.

[10] James H Marshel et al. “Targeting single neuronal networks for gene expression and cell labeling in vivo”. In: *Neuron* 67.4 (2010), pp. 562–574.

[11] Anne M Taylor et al. “Microfluidic multicompartment device for neuroscience research”. In: *Langmuir* 19.5 (2003), pp. 1551–1556.

[12] Isabel Yasmin Buchsbaum and Silvia Cappello. “Neuronal migration in the CNS during development and disease: insights from in vivo and in vitro models”. In: *Development* 146.1 (2019), dev163766.

[13] Paul M Holloway et al. “Advances in microfluidic in vitro systems for neurological disease modeling”. In: *Journal of neuroscience research* 99.5 (2021), pp. 1276–1307.

[14] Jason M Keller and Monica Frega. “Past, present, and future of neuronal models in vitro”. In: *In Vitro Neuronal Networks: From Culturing Methods to Neuro-Technological Applications* (2019), pp. 3–17.

[15] Kazutoshi Takahashi and Shinya Yamanaka. “Induction of pluripotent stem cells from mouse embryonic and adult fibroblast cultures by defined factors”. In: *cell* 126.4 (2006), pp. 663–676.

[16] Hui Huang et al. “Using microfluidic chip to form brain-derived neurotrophic factor concentration gradient for studying neuron axon guidance”. In: *Biomicrofluidics* 8.1 (2014).

[17] Holger Fehlauer et al. “Using a Microfluidics Device for Mechanical Stimulation and High Resolution Imaging of C. elegans”. In: *Journal of Visualized Experiments* 2018 (Feb. 2018). DOI: 10.3791/56530.

[18] Paolo Massobrio et al. “In vitro studies of neuronal networks and synaptic plasticity in invertebrates and in mammals using multielectrode arrays”. In: *Neural plasticity* 2015.1 (2015), p. 196195.

[19] Sol Ah Lee et al. “Dynamic temperature control in microfluidics for in vivo imaging of cold-sensing in C. elegans”. In: *Biophysical Journal* 123.8 (2024), pp. 947–956.

[20] Jeroen Rouwkema et al. “In vitro platforms for tissue engineering: implications for basic research and clinical translation”. In: *Journal of tissue engineering and regenerative medicine* 5.8 (2011), e164–e167.

[21] Pamela G Gross et al. “Applications of microfluidics for neuronal studies”. In: *Journal of the neurological sciences* 252.2 (2007), pp. 135–143.

[22] Luís F Martins et al. “Mesenchymal stem cells secretome-induced axonal outgrowth is mediated by BDNF”. In: *Scientific reports* 7.1 (2017), p. 4153.

[23] Kangning Ren, Jianhua Zhou, and Hongkai Wu. “Materials for microfluidic chip fabrication”. In: *Accounts of chemical research* 46.11 (2013), pp. 2396–2406.

[24] Rachelle N Palchesko et al. “Development of polydimethylsiloxane substrates with tunable elastic modulus to study cell mechanobiology in muscle and nerve”. In: *PloS one* 7.12 (2012), e51499.

[25] Rupam Das, Farshad Moradi, and Hadi Heidari. “Biointegrated and wirelessly powered implantable brain devices: A review”. In: *IEEE transactions on biomedical circuits and systems* 14.2 (2020), pp. 343–358.

[26] Anne M Taylor et al. “A microfluidic culture platform for CNS axonal injury, regeneration and transport”. In: *Nature methods* 2.8 (2005), pp. 599–605.

[27] Rouhollah Habibey et al. “A microchannel device tailored to laser axotomy and long-term microelectrode array electrophysiology of functional regeneration”. In: *Lab on a chip* 15.24 (2015), pp. 4578–4590.

[28] Suneil Hosmane et al. “Valve-based microfluidic compression platform: single axon injury and regrowth”. In: *Lab on a Chip* 11.22 (2011), pp. 3888–3895.

[29] Eve Moutaux et al. “Neuronal network maturation differently affects secretory vesicles and mitochondria transport in axons”. In: *Scientific reports* 8.1 (2018), p. 13429.

[30] Kiran Raj M and Suman Chakraborty. “PDMS microfluidics: A mini review”. In: *Journal of Applied Polymer Science* 137.27 (2020), p. 48958.

[31] Veronika Truxova et al. “Ceramic 3D printing: Comparison of SLA and DLP technologies”. In: *MM Sci. J* 2020 (2020), pp. 3905–3911.

[32] Bastien Venzac et al. “PDMS curing inhibition on 3D-printed molds: why? Also, how to avoid it?” In: *Analytical chemistry* 93.19 (2021), pp. 7180–7187.

[33] Yun Li and Bo Li. “Direct ink writing 3D printing of polydimethylsiloxane-based soft and composite materials: a mini review”. In: *Oxford Open Materials Science* 2.1 (2022), itac008.

[34] MASR Saadi et al. “Direct ink writing: a 3D printing technology for diverse materials”. In: *Advanced Materials* 34.28 (2022), p. 2108855.

[35] Veli Ozbolat et al. “3D printing of PDMS improves its mechanical and cell adhesion properties”. In: *ACS Biomaterials Science & Engineering* 4.2 (2018), pp. 682–693.

[36] Zhenyu Wang et al. “3D-printed graphene/polydimethylsiloxane composites for stretchable and strain-insensitive temperature sensors”. In: *ACS applied materials & interfaces* 11.1 (2018), pp. 1344–1352.

[37] Mohammad Abshirini et al. “3D printing of highly stretchable strain sensors based on carbon nanotube nanocomposites”. In: *Advanced Engineering Materials* 20.10 (2018), p. 1800425.

[38] Kang Xu et al. “A heating-assisted direct ink writing method for preparation of PDMS cellular structure with high manufacturing fidelity”. In: *Polymers* 14.7 (2022), p. 1323.

[39] Ruifeng Jiang et al. “Direct write printing of ultraviolet-curable bulk superhydrophobic ink material”. In: *ACS Applied Materials & Interfaces* 15.44 (2023), pp. 52000–52009.

[40] Yuan Xiao et al. “Preparation of graphene/polydimethylsiloxane flexible resistive pressure sensors based on direct ink writing 3D printing”. In: *Sensors and Actuators A: Physical* 382 (2025), p. 116148.

[41] Ge Shi et al. “A versatile PDMS submicrobead/graphene oxide nanocomposite ink for the direct ink writing of wearable micron-scale tactile sensors”. In: *Applied Materials Today* 16 (2019), pp. 482–492.

[42] Katherine A Southam et al. “Microfluidic primary culture model of the lower motor neuron–neuromuscular junction circuit”. In: *Journal of neuroscience methods* 218.2 (2013), pp. 164–169.

[43] I. H. Yang, D. Gary, M. Malone, et al. “Axon Myelination and Electrical Stimulation in a Microfluidic, Compartmentalized Cell Culture Platform”. In: *Neuromolecular Medicine* 14 (2012), pp. 112–118. DOI: 10.1007/s12017-012-8170-5. URL: https://doi.org/10.1007/s12017-012-8170-5.

[44] S. Scott and Z. Ali. “Fabrication Methods for Microfluidic Devices: An Overview”. In: *Micromachines (Basel)* 12.3 (Mar. 2021), p. 319. DOI: 10.3390/mi12030319. URL: https://doi.org/10.3390/mi12030319.

[45] L. Yildirimer et al. “Engineering three-dimensional microenvironments towards in vitro disease models of the central nervous system”. In: *Biofabrication* 11.3 (June 2019), p. 032003. DOI: 10.1088/1758-5090/ab17aa.

[46] Y.-C. Kung et al. “Fabrication of 3D high aspect ratio PDMS microfluidic networks with a hybrid stamp”. In: *Lab on a Chip* 15.8 (2015), pp. 1861–1868. DOI: 10.1039/C4LC01211A.

[47] J. D. Williams. “Study on the postbaking process and the effects on UV lithography of high aspect ratio SU-8 microstructures”. In: *Journal of Micro/Nanolithography, MEMS, and MOEMS* 3.4 (Oct. 2004), p. 563. DOI: 10.1117/1.1792650.

[48] H. V. Jansen et al. “Black silicon method: X. A review on high speed and selective plasma etching of silicon with profile control: an in-depth comparison between Bosch and cryostat DRIE processes as a roadmap to next generation equipment”. In: *Journal of Micromechanics and Microengineering* 19.3 (Mar. 2009), p. 033001. DOI: 10.1088/0960-1317/19/3/033001.

[49] L. Gitlin, P. Schulze, and D. Belder. “Rapid replication of master structures by double casting with PDMS”. In: *Lab on a Chip* 9.20 (2009), p. 3000. DOI: 10.1039/b904684d.

[50] L. Sifringer et al. “An implantable biohybrid nerve model towards synaptic deep brain stimulation”. In: (June 2024). DOI: 10.1101/2024.05.31.596665.

[51] K. Vulić et al. “Impact of microchannel width on axons for brain-on-chip applications”. In: *Lab on a Chip* 24.22 (2024), pp. 5155–5166. DOI: 10.1039/D4LC00440J.

[52] S. K. Ammu et al. “3D Printing of Lead□Free Piezoelectric Ultrasound Transducers”. In: *Advanced Materials Technologies* 9.23 (Dec. 2024). DOI: 10.1002/admt.202400858.

[53] C. Y. Hui et al. “Constraints on Microcontact Printing Imposed by Stamp Deformation”. In: *Langmuir* 18.4 (Feb. 2002), pp. 1394–1407. DOI: 10.1021/la0113567.

A

Microfabrication Flowchart

STARTING MATERIAL

Use wafers / substrates with the following specifications:

Type:	Regular silicon Wafer (SSB)
Orientation:	$<100>$, 0 deg off orientation
Resistivity:	Any
Thickness:	525 ± 15 μm
Diameter:	100.0 ± 0.2 mm

If the wafers / substrates are taken out of an unopened wafer box, no cleaning will be necessary.
Wafers / substrates taken from an already opened box must be cleaned following the standard procedure.

Step 1: Cleaning

Tool(s)	Wet bench; HNO_3 modules (99% and 69.5% at 110°C); QDR; Avenger Ultra Pure-6 rinse/dry tool
Location	Class 100 tunnel 5
Manual	Manual operation for the HNO_3 modules
Recipe	Default recipe for the Avenger Ultra Pure-6 rinse/dry tool
Settings	Use the white wafer carrier labelled with the red dot for HNO_3 99%, Rinse 1, HNO_3 69.5%, and Rinse 2; use the wafer carrier with the red dot for Rinse 3. Verify HNO_3 69.5% bath temperature is 110°C.

Step 2: Oxide Deposition

Tool(s)	Novellus Concept 1
Location	CR 100 – Tunnel 3 (Plasma)
Recipe	.xxxsiostd
Settings	Ensure the gas switch is ON (see wall instructions). Press F10 $\rightarrow$ Group $\rightarrow$ undoped oxides $\rightarrow$ select `.xxxsiostd`. Set deposition time to 30 s to deposit $\sim$2500 nm SiO_2. Open the door, load cassette (no empty slots), close door, press F10, enter wafer count, then press GO.

Step 3: Photoresist Coating (positive mold)

Tool(s)	EVG120 system
Location	Class 100 tunnel 1B
Manual	See printed manual at the module
Recipe	1 Co - 3027 - 3.1 μm - no EBR
Settings	**Adhesion promotion:** EVG120 `1-Only HMDS` on coater 50 s, or manual HMDS vapor priming 10 min. **Spin coating:** 700 rpm (accel 1000 rpm/s); dispense 3 mL AZ ECI 3027; ramp to 2840 rpm (accel 1750 rpm/s); spin 30 s; stop (decel 5000 rpm/s). **Soft bake:** 95°C for 30 s at 500 μm proximity, then 100 μm for 90 s.

Step 4: Pattern Exposure

Tool(s)	SUSS MicroTec MA/BA8 Mask Aligner
Location	Class 100 tunnel 1B
Manual	See printed manual at the module
Recipe	1_FSA_Hard_Contact
Settings	Lamp temperature 55°C; lamp power 999/1000 W. Follow the manual: adjust WEC pressure until the dial is within $\pm$1.0 kPa of the value on the chuck. Compute exposure time from required dose and lamp output.

Step 5: Photoresist Development (positive mold)

Tool(s)	EVG120 system (developer station)
Location	Class 100 tunnel 1B
Manual	See printed manual at the module
Recipe	1-Dev-DP 1
Settings	Post-exposure bake 115°C for 90 s; develop in Shipley MF322 using double puddle process; hard bake 100°C for 90 s. Always follow on-tool instructions.

Step 6: Reactive Ion Etching (RIE)

Tool(s)	Drytek Triode 384T
Location	Class 100 tunnel 3
Settings	Etch rate $\approx$600 nm/min. For a 3000 nm layer, etch $\sim$5 min with $\sim$10% over-etch to ensure full clearance.

Step 7: Deep Reactive Ion Etching (DRIE)

Tool(s)	Rapier Omega i2L DRIE etcher
Location	CR 100 – Tunnel 2
Manual	See printed manual at the module
Recipe	0EKL_Smooth_20C_xxx
Settings	Log in $\rightarrow$ VCH $\rightarrow$ Eject; load wafer and close door. Select Recipe $\rightarrow$ waferview. Etch rate $\approx$0.72 μm per loop; for 100 μm depth, set about 139 loops.

Photoresist Coating (negative mold)

Tool(s)	EVG120 system
Location	Class 100 tunnel 1B
Manual	See printed manual at the module
Recipe	1 Co - Nlof - 3.0 μm - no EBR
Settings	**Adhesion promotion:** EVG120 `1-Only HMDS` (50 s) or manual HMDS vapor prime (10 min). **Spin coating:** 700 rpm (accel 1000 rpm/s); dispense 2.6 mL AZ nLOF 2020; ramp to 1500 rpm (accel 1500 rpm/s); spin 30 s; stop (decel 5000 rpm/s). **Soft bake:** 95°C for 30 s at 1000 μm proximity, then 100 μm for 105 s.

Photoresist Development (negative mold)

Tool(s)	EVG120 system (developer station)
Location	Class 100 tunnel 1B
Manual	See printed manual at the module
Recipe	1-Dev-lift off
Settings	**Double-puddle develop:** Dispense MF-322 to form a puddle; wait 75 s; rinse thoroughly with DI water ($\geq$10 s). (Optional) spin-dry. Repeat once (second puddle 75 s); rinse $\geq$10 s; spin-dry. **Hard bake:** 100°C for 90 s at 100 μm proximity.

B

Additional Figures

B.1. 3D-Printed Structures Under Different Printing Parameters

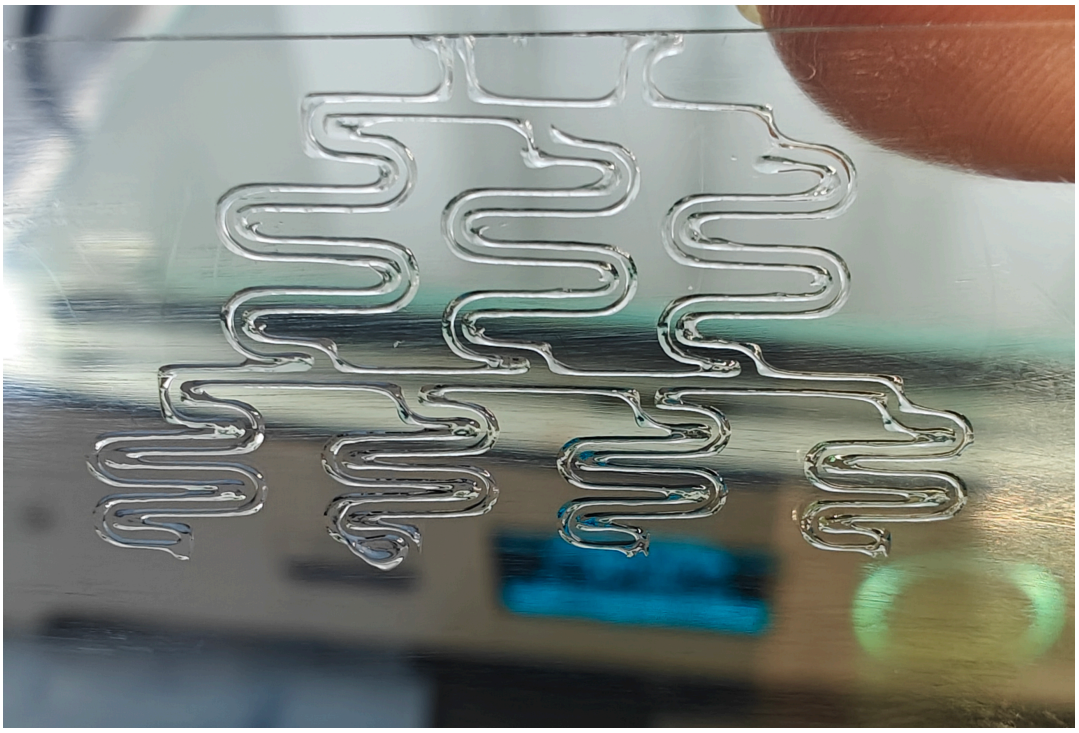

Figure B.1: Ink:9:1, nozzle size:210μm, displacement 0.1mm, printing speed 10mm/s

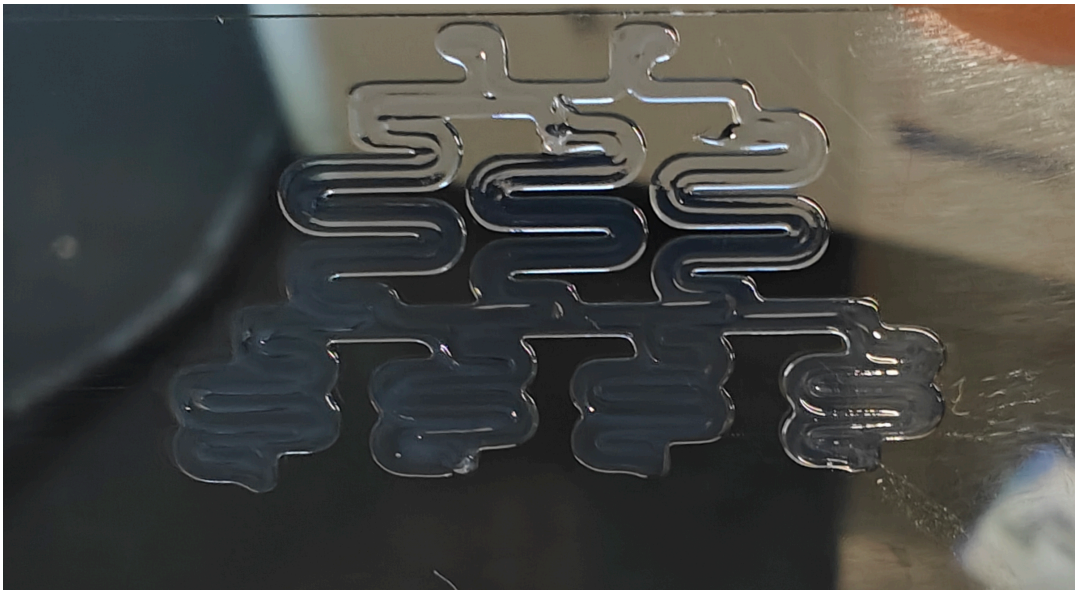

Figure B.2: Ink:8:2, nozzle size:210µm, displacement 0.4mm, printing speed 5mm/s

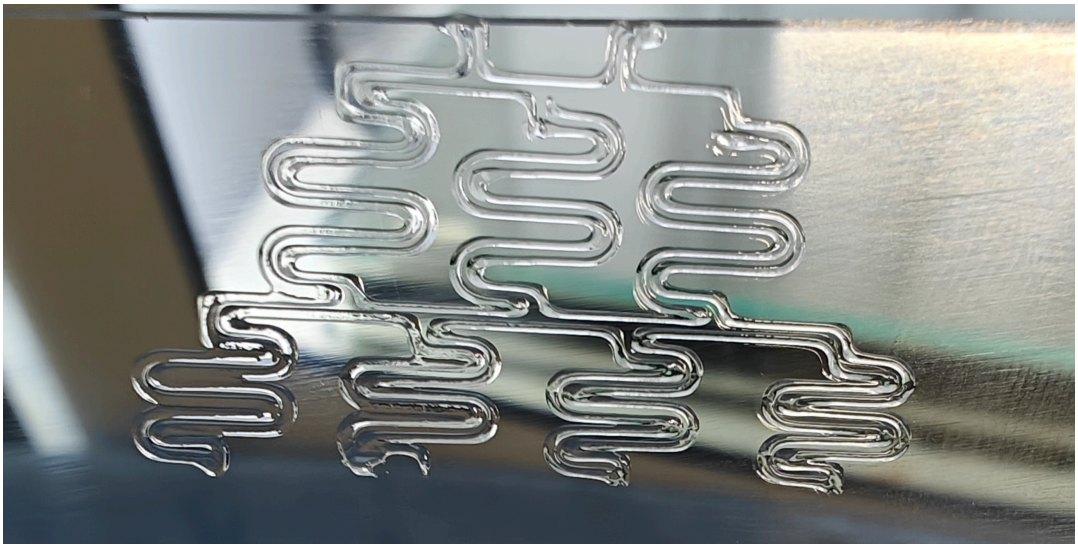

Figure B.3: Ink:8:2, nozzle size:210µm, displacement 0.4mm, printing speed 10mm/s

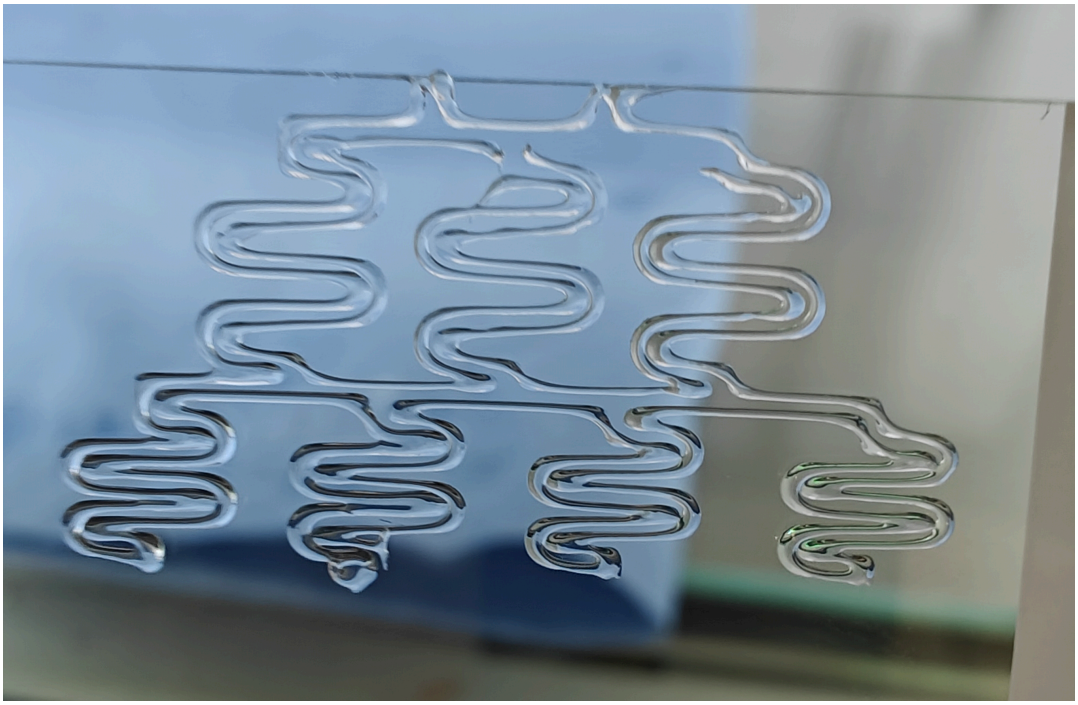

Figure B.4: Ink:8:2, nozzle size:210µm, displacement 0.4mm, printing speed 15mm/s

B.2. SEM Images of the 5µm Wafer Mold

Previous 3D images from the confocal microscope suggested that the adjacent pillars appeared to be connected, and here clearer SEM images are provided.

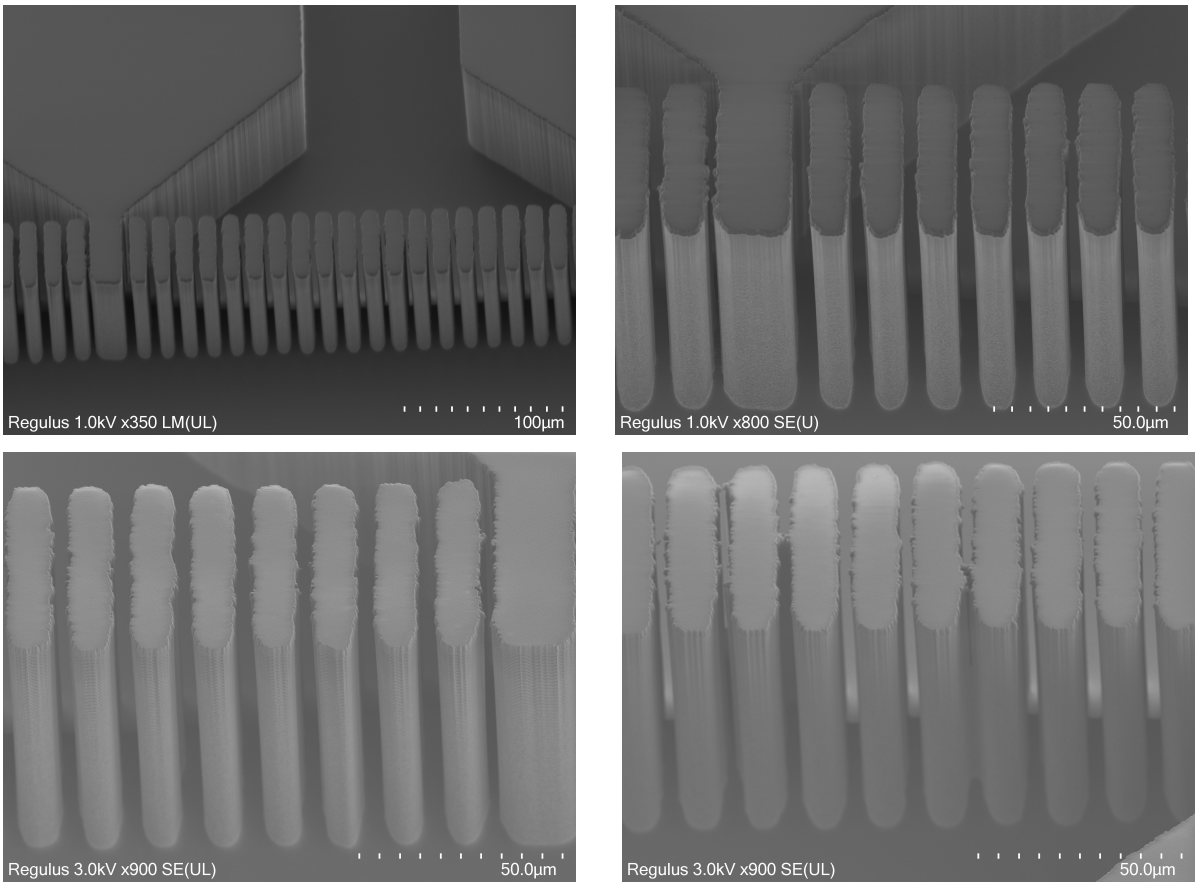

Figure B.5: SEM images of the 5µm wafer mold

B.3. Demolding Failure Cases

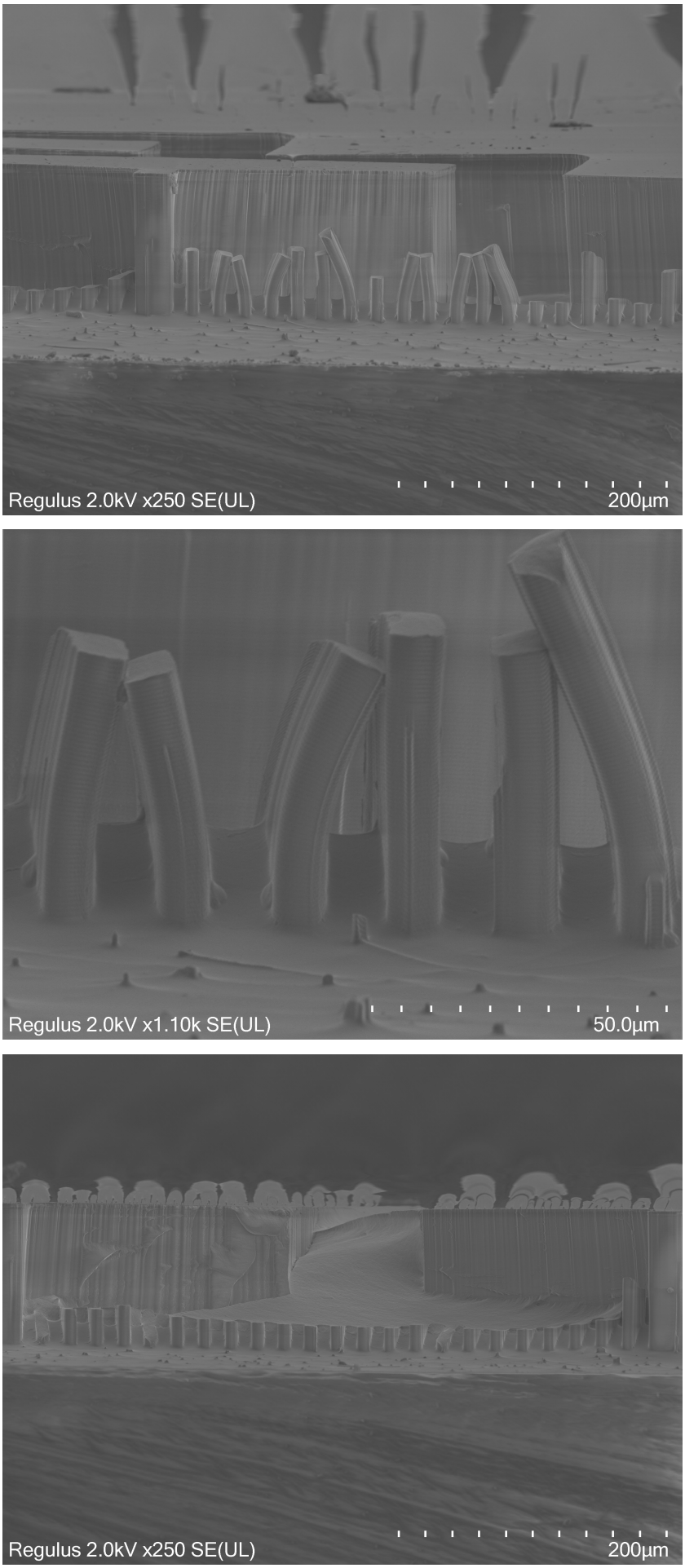

Figure B.6: Demolding Failure Cases

B.4. Aspect Ratio of Wafer Molds

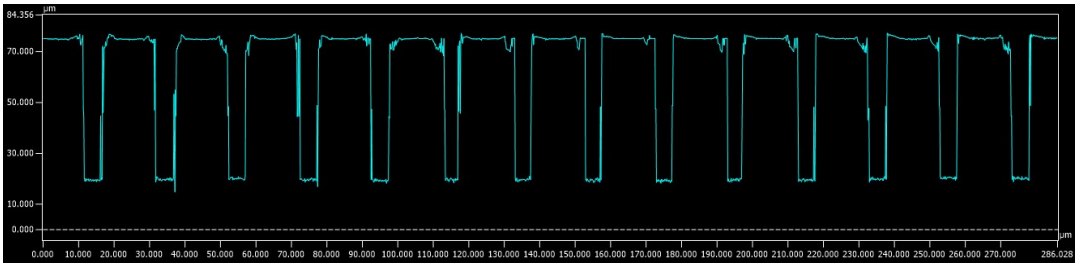

Figure B.7: Cross-sectional view of the 10 µm negative mold cell body blocking channels

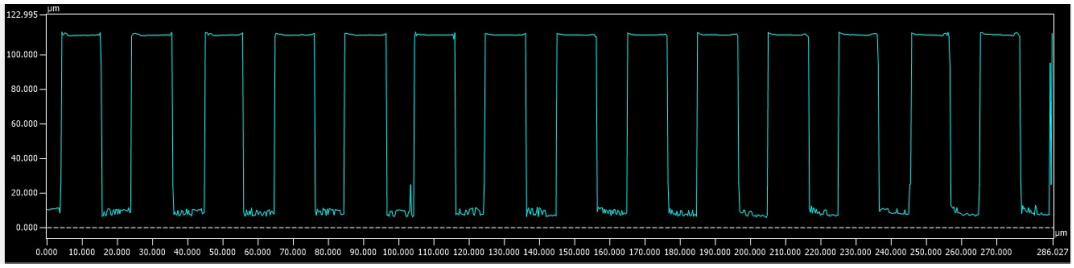

Figure B.8: Cross-sectional view of the 10 µm positive mold cell body blocking channels

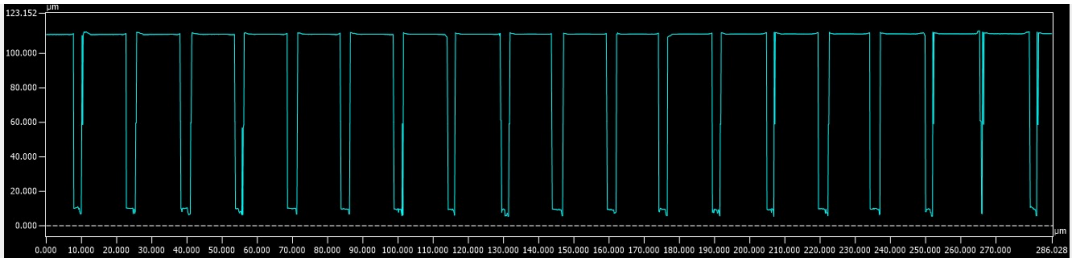

Figure B.9: Cross-sectional view of the 5 µm positive mold cell body blocking channels

C

Another Ultimaker Cura Settings

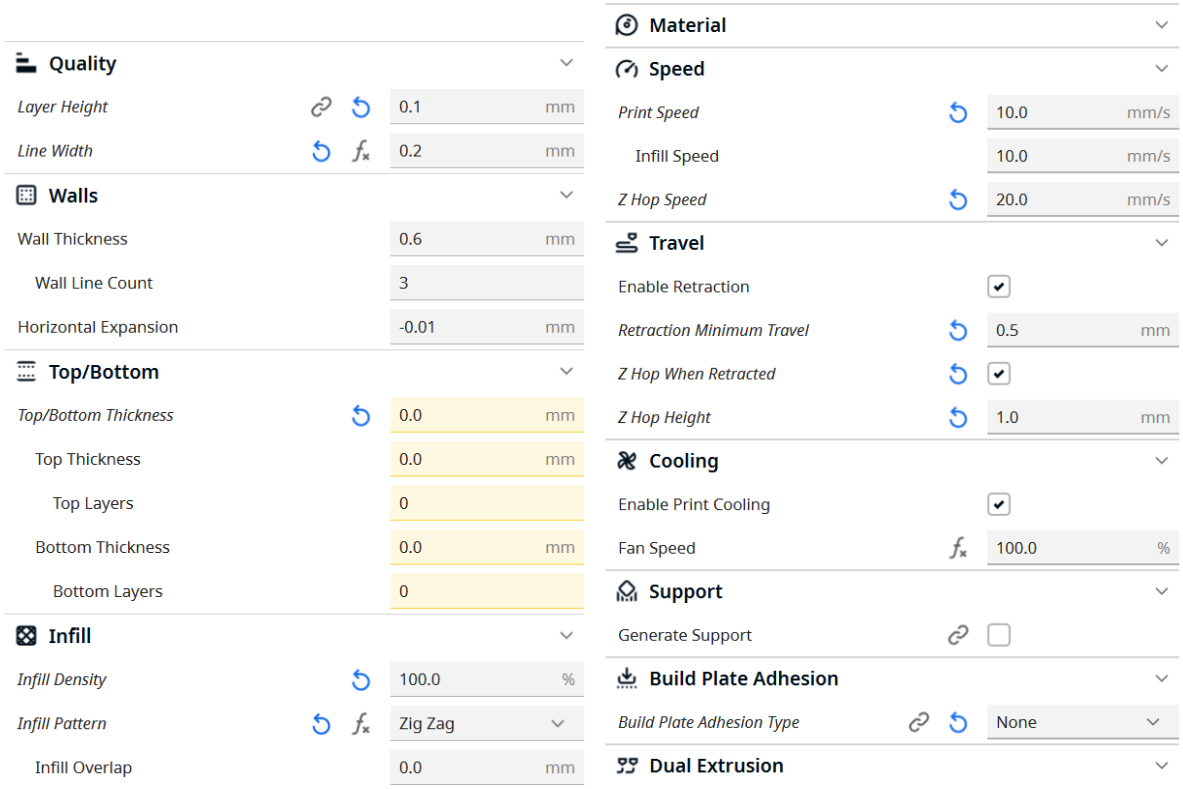

Figure C.1: Another Ultimaker Cura settings

The above are additional settings used for DIW printing of PDMS ink. Apart from the printing speed, these settings have little effect on the width of a single filament but can influence the overall printing quality of the object.

The Line Width needs to match the actual size of the printed filament to avoid distortion. In the case of a single filament structure (only one line without a surface), the concept of Wall is almost meaningless, as there is no enclosed outer wall. At the same time, the values of Layer Height and Top/Bottom also do not affect the structure. Retraction is only performed when the print head moves more than 0.5 mm. During retraction, the nozzle lifts in the Z direction to avoid scratching the already printed structure. Since PDMS is not thermally extruded, Cooling is in fact ineffective. Setting Build Plate Adhesion to None during printing can prevent interference from additional material.